UNIVERSITY OF JYVÄSKYLÄ
DEPARTMENT OF CHEMISTRY

RESEARCH REPORT NO. 171

LIISA ANTILA

SPECTROSCOPIC STUDIES OF ELECTRON TRANSFER REACTIONS AT THE PHOTOACTIVE ELECTRODE OF DYE-SENSITIZED SOLAR CELLS.

Academic Dissertation for
the Degree of Doctor of Philosophy

UNIVERSITY OF JYVÄSKYLÄ
2013

DEPARTMENT OF CHEMISTRY, UNIVERSITY OF JYVÄSKYLÄ RESEARCH REPORT No. 171

SPECTROSCOPIC STUDIES OF ELECTRON TRANSFER REACTIONS AT THE PHOTOACTIVE ELECTRODE OF DYE-SENSITIZED SOLAR CELLS.

BY

LIISA ANTILA

Academic Dissertation for the Degree of
Doctor of Philosophy

To be presented, by permission of the Faculty of Mathematics and Science of the University of Jyväskylä, for public examination in Auditorium YAA303, on September 20th , 2013 at 12 noon.

UNIVERSITY OF JYVÄSKYLÄ

Jyväskylä, Finland
ISBN 978-951-39-5352-2
ISSN 0357-346X

URN:ISBN:978-952-86-0223-1
ISBN 978-952-86-0223-1 (PDF)
ISSN 0357-346X

University of Jyväskylä, 2024

ABSTRACT

Antila Liisa
Spectroscopic studies of electron transfer reactions at the photoactive electrode of dye-sensitized solar cells.
Jyväskylä: University of Jyväskylä, 2013, 63 p.
(Department of Chemistry, University of Jyväskylä Research Report
ISSN 0357-346X, 171)
ISBN 978-951-39-5352-2
Diss.

Harnessing solar energy is a key issue in solving the global energy challenge. The Sun's radiant energy can be converted into electricity by photovoltaics. One of the most promising, emerging PV technologies is the dye-sensitized solar cell. In order to develop this technology, understanding the dynamics of charge separation and electron transfer reactions in the cell is of fundamental importance. In this thesis, rates of electron transfer in dye-sensitized titanium dioxide films and complete solar cells were investigated by means of transient absorption and transient emission spectroscopies, as well as with electrochemical impedance spectroscopy. The effect of altering electron transfer rates on the performance of the cells was monitored by recording the current-voltage response of the cells under simulated sunlight.

Electron transfer from two ruthenium dyes to titanium dioxide film (electron injection) in neat solvent and in the presence of an iodide/triiodide electrolyte was studied by following the ultrafast temporal evolutions of the absorptions of oxidized dye and of injected electrons. Electron injection was found to be almost two orders of magnitude slower in the presence of the complete electrolyte compared to injection in neat solvent. Comparison of the transient absorption signals of the oxidized dye and injected electrons of the sensitized TiO_2 films in contact with the I^-/I_3^- electrolyte revealed the picosecond time scale of dye regeneration for the first time, twenty years after the invention of the cell. This observation also paves the way for understanding the detailed molecular mechanisms of the function of the electrolyte redox couple in the cell.

Metal oxide barrier layers deposited on the nanocrystalline TiO_2 film were studied as a means to improve cell performance. The desired effect of the barrier layer is to slow down recombination reactions while maintaining good electron injection efficiency. Barrier layers were prepared with atomic layer deposition for better controllability of layer thickness and morphology. Aluminum oxide was found to slow down injection more than recombination, which led to deterioration of cell performance. Hafnium oxide barriers up to four atomic layer cycles retarded injection much less than the corresponding aluminum oxide layers, and in practice, retained cell performance. According to this result, increasing hafnium oxide layer thickness and improving its penetration into TiO_2 film would provide a means to improve cell performance.

Surprisingly, a relatively thick (about 1nm) tantalum oxide coating resulted in enhancement of the injection efficiency and led to about a 10% increase in the current output of the cell. This finding was significant as no barrier layer on TiO_2 so far has been reported to have shown an increase in injection efficiency. More interestingly, improved cell performance was obtained for the TiO_2 film with only the top quarter of the film covered with tantalum oxide.

Keywords: dye-sensitized solar cell, barrier layer, electron injection, regeneration, recombination, atomic layer deposition, transient absorption spectroscopy, time-correlated single photon counting, electrochemical impedance spectroscopy

Author's address

Liisa Antila
Nanoscience Center
Department of Chemistry
University of Jyväskylä
P.O.Box 35
FI-40014 University of Jyväskylä
liisa.j.antila@jyu.fi

Supervisor

Prof. Jouko Korppi-Tommola
Nanoscience Center
Department of Chemistry
University of Jyväskylä
P.O.Box 35
FI-40014 University of Jyväskylä
jouko.korppi-tommola@jyu.fi

Reviewers

Prof. Nikolai V. Tkachenko
Department of Chemistry and Bioengineering
Tampere University of Technology
Finland

Prof. Peter Lund
Department of Applied Physics
Aalto University School of Science
Finland

Opponent

Prof. Leif Hammarström
Department of Photochemistry and Molecular Science
Uppsala University
Sweden

ACKNOWLEDGEMENTS

The work presented in this thesis has been carried out at the Department of Chemistry, Nanoscience Center at the University of Jyväskylä during the years 2007–2013. The work has been financially supported by the Graduate School of Computational Chemistry and Molecular Spectroscopy (LASKEMO), the Magnus Ehrnrooth Foundation, the Academy of Finland, and the Department of Chemistry, which are all gratefully acknowledged.

I would like to thank my supervisor Prof. Jouko Korppi-Tommola for offering me the opportunity to become a researcher and work in the interesting field of dye-sensitized solar cells. I have learned many valuable lessons on conducting scientific research. I also want express my gratitude for the invaluable help and advice from Dr. Pasi Myllyperkiö, Dr. Viivi Aumanen, Dr. Heli Lehtivuori, docent Karoliina Honkala, and docent Jussi Toppari.

The work could not have been accomplished without collaboration: I thank the group of Prof. Markku Leskelä at the University of Helsinki for the numerous ALD-coatings and the group of Prof. Mika Valden at Tampere University of Technology for XPS and UPS measurements. I also wish to thank Prof. Nikolai Tkachenko at Tampere University of Technology for the opportunity to conduct flash photolysis experiments in his lab and for the inspiring discussions. Dr. Muhammad Imran Asghar is acknowledged for his advice and friendship. In-house collaborators Dr. Ville Mäkinen and docent Karoliina Honkala are thanked for the DFT calculations in Paper III. I am also grateful for the help from the group of docent Jussi Toppari in performing the EIS and IPCE measurements. MSc Mikko Laitinen and docent Timo Sajavaara are acknowledged for the RBS and ToF-ERDA measurements and analysis.

I have been privileged to work in an exceptionally inspiring and warmhearted atmosphere in the Nanoscience Center and in the Department of Chemistry. I wish to thank my past and present coworkers and especially the colleagues from the Physical Chemistry Department for their support and for the fun moments we have shared. The friendship of Dr. Anni Siitonen, Dr. Hanna Tikkanen, Dr. Eero Hulkko, and Dr. Heli Lehtivuori has meant a lot to me.

All work and no play would make life dull. I am grateful to the people of Chamber Choir Cantinovum and all my other friends for making my life more exciting. I thank my family for their love and encouragement, and my husband Sami for being my rock.

Jyväskylä, August 2013

Liisa Antila

LIST OF ORIGINAL PUBLICATIONS

This thesis reviews the original publications and the manuscript listed below, and they are herein referred to by their Roman numerals.

I. L. Antila, S. Mustalahti, H. Lehtivuori, P. Myllyperkiö, J. Korppi-Tommola: **"Electron injection studies of dye-sensitized TiO_2 films in solvent and in iodide/triiodide electrolyte: Evidence of dye regeneration in the picosecond timescale"** submitted to Journal of American Chemical Society.
https://doi.org/10.1021/jp4124277

II. L. Antila, M. Heikkilä, P. Jalkanen, V. Aumanen, P. Myllyperkiö, M. Kemell, M. Leskelä, J. Korppi-Tommola: **" Suppression of forward electron injection from $Ru(dcbpy)_2(NCS)_2$ to nanocrystalline TiO_2 film as a result of interfacial Al_2O_3 barrier layer prepared with atomic layer deposition"**, J. Phys. Chem. Lett. 2010 (1), 536-539.
https://doi.org/10.1021/jz9003075

III. L. Antila, M. Heikkilä, V. Mäkinen, N. Humalamäki, M. Laitinen, V. Linko, P. Jalkanen, J. Toppari, V. Aumanen, M. Kemell, P. Myllyperkiö, K. Honkala, H. Häkkinen, M. Leskelä, J. Korppi-Tommola: **"ALD Grown Aluminum Oxide Submonolayers in Dye-Sensitized Solar Cells: The Effect on Interfacial Electron Transfer and Performance"**, The Journal of Physical Chemistry C 2011, 115, 16720-16729.
https://doi.org/10.1021/jp204886n

The author has carried out all sample preparations except the atomic layer deposition of metal oxide layers. Optical and electrochemical spectroscopic measurements and analysis of the experimental results were conducted by the author, excluding the measurements employing mid-infrared probing. The author has written the first drafts for all listed papers. In Chapter 3, unpublished results for hafnium and tantalum oxide barrier coating are presented. This work was carried out fully by the author.

ABBREVIATIONS

ADC	analog-to-digital converter
ALD	atomic layer deposition
CB	conduction band
CFD	constant-fraction discriminator
CPE	constant phase element
DFT	density functional theory
DSC	dye-sensitized solar cell
EA	electron affinity
EDX	energy-dispersive X-ray spectrometry
EIS	electrochemical impedance spectroscopy
ET	electron transfer
FE	free energy
FF	fill factor
FTO	fluorine doped tin oxide
FWHM	full width at half maximum
GPC	growth-per-cycle
GuSCN	guanidium thiocyanate
HOMO	highest occupied molecular orbital
HRTEM	high-resolution transmission electron microscope
IPCE	incident-photon-to-current conversion efficiency
IRF	instrument response function
ISC	intersystem crossing
IV	current-voltage
LHE	light-harvesting efficiency
LMCT	ligand-to-metal charge transfer
LUMO	lowest unoccupied molecular orbital
MBI	N-methyl benzimidazolium
MLCT	metal-to-ligand charge transfer
MPN	3-methoxypropionitrile
NHE	normal hydrogen electrode
NOPA	noncollinear parametric amplification
PZC	point of zero charge
RBS	Rutherford back-scattering spectrometry
REELS	reflective electron energy loss spectroscopy
TA	transient absorption
TAC	time-to-amplitude converter
TBP	*tert*-butylpyridine
TCSPC	time-correlated single photon counting
TEMAH	tetrakis(ethylmethylamino) hafnium
TMA	trimethylaluminum

ToF-ERDA	time-of-flight elastic recoil detection analysis
UPS	ultraviolet photon spectroscopy
VBM	valence band maximum

CONTENTS

1 INTRODUCTION

The annual world energy consumption in 2010 was 148,000 TWh[1] and is estimated to increase to 170–230 000 TWh by 2035.[1, 2] Meeting this demand solely with fossil fuels and nuclear energy is impossible: With the current level of consumption, the world's fossil fuel reserve is going to be depleted in 100 years' time.[3] Hundreds of GW-level nuclear plants would need to be built (current capacity 8430 TWh),[1] while the question of disposing of nuclear waste is still unresolved. Additionally, the Fukushima nuclear accident has led many developed countries like Germany and Japan to abandon nuclear power altogether. Renewable energy must thus have a significant role in future energy production. The Sun is an abundant energy source (about 885 million TWh reach Earth's surface per year), and harnessing solar energy effectively is a key issue in solving the global energy challenge.

The first single crystal silicon solar cell was prepared in Bell labs in 1954.[4] The first practical application of solar cell technology was as a power source of satellites, and thus reliability and efficiency were more important than cost. In the seventies, multicrystalline silicon solar cells were invented and were followed by binary semiconductor cells combining II-IV and IIIV group elements.[5] From the first generation of solar cells, silicon-based cells have become by far commercially most important. They present rather high conversion efficiencies of 20–30% and used to suffer from high material costs and energy intensive production. During last five years, however, prices have fallen dramatically to 1.5$ per peak watt (W_p) in 2011 from 5-6$ five years ago and are confidently expected to go below 1$/$W_p$ in the coming years. In second-generation solar cells, material costs were cut by using very thin films of amorphous silicon, CIGS (copper indium gallium selenide), and CdTe. These devices typically reach conversion efficiencies of 10–20%, and the price level of 1$/$W_p$ has been obtained. However, truly low-cost (0.5$/$W_p$) solar cell technology was introduced in the third-generation solar cells, which can be made of inexpensive materials and are well-suited for mass production. These cells are not restricted by the Shockley-Queisser limit (31%), which dictates that one absorbed photon will produce one electron-hole pair, and all of the photon energy exceeding the

band gap will be lost as heat. Cells that have exceeded the 31% efficiency limit include, e.g., tandem, hot-carrier, and multiexciton generation cells. Dye-sensitized solar cells (DSCs), organic polymer heterojunction solar cells, and quantum dot cells are often considered as belonging to the third generation though their recorded efficiencies so far are more modest (around 10%). However, DSC technology has already become commercially viable. The benefits of DSCs compared to silicon-based solar cells in addition to their low cost are, among others, better performance under low- and diffuse-light conditions and at elevated temperatures, lightweight, and flexibility.

The DSC was introduced in 1991 in a Nature paper by Brian O'Regan and Michael Grätzel,[6] and since then, a huge scientific effort (more than 7500 publications since 1990 according to Web of Science) has been made in order to understand the fundamental physical mechanisms of these cells and to improve their conversion efficiencies. Despite this great effort, it has taken 20 years for substantial breakthroughs to take place. In 2011, a record of 12.4% conversion efficiency was reported. Introducing a new type of dye and a new redox couple with an open circuit voltage of 1 volt was reached.[7] Another important breakthrough was achieved in 2012. A new record efficiency of 10.2% for a solid state DSC using a completely new type of hole transport perovskite material $CsSnI_3$ was reported.[8] This gives promise for extended lifetime for DSCs as compared to previous cells using liquid electrolyte. Quite recently, a new record of 14.4% of a liquid electrolyte-based DSC has been announced.[9] The latest breakthrough was realized by the introduction of a hybrid perovskite pigment as a sensitizer to obtain nearly a 15% conversion efficiency of the DSC.[10]

Dye-sensitized solar cells function in principle the same way as photosynthesis, by absorbing sunlight and converting it to energy. While photosynthesis produces chemical energy, a DSC produces electricity. A dye-sensitized solar cell has a photoactive electrode and a counter electrode (Figure 1). The photoactive electrode consists of a nanocrystalline semiconductor film on a substrate with a conductive FTO layer (fluorine doped tin oxide, $F:SnO_2$). The semiconductor film is typically 10–15 μm thick and is composed of 10–20 nm diameter particles to ensure a high surface area, which enables efficient sensitization of the film by the covalent binding of a large number of dye molecules. The photoactive electrode is glued with a Surlyn spacer frame to the counter electrode, which is another piece of FTO glass coated with a catalyst layer. An electrolyte containing a redox couple fills the space between the electrodes. The electrolyte has a high ionic strength and often contains additives to improve the cell performance. A wide range of materials and methods have been used in the preparation of dye-sensitized solar cells, and interested readers can refer to the review article by Hagfeldt et al.[5] or to the book by Kalyanasundaram.[11] In this work, the photoactive electrode was composed of titanium dioxide (TiO_2) sensitized with a ruthenium bipyridyl dye N3 ($Ru(dcbpy)_2(NCS)_2$, dcbpy = 4,4′-dicarboxy-2,2′-bipyridine[12]) or its di-TBA salt N719.[13] The catalyst on the counter electrode was platinum, and the electrolyte contained an I^-/I_3^- redox couple in 3-methoxypropionitrile (MPN).

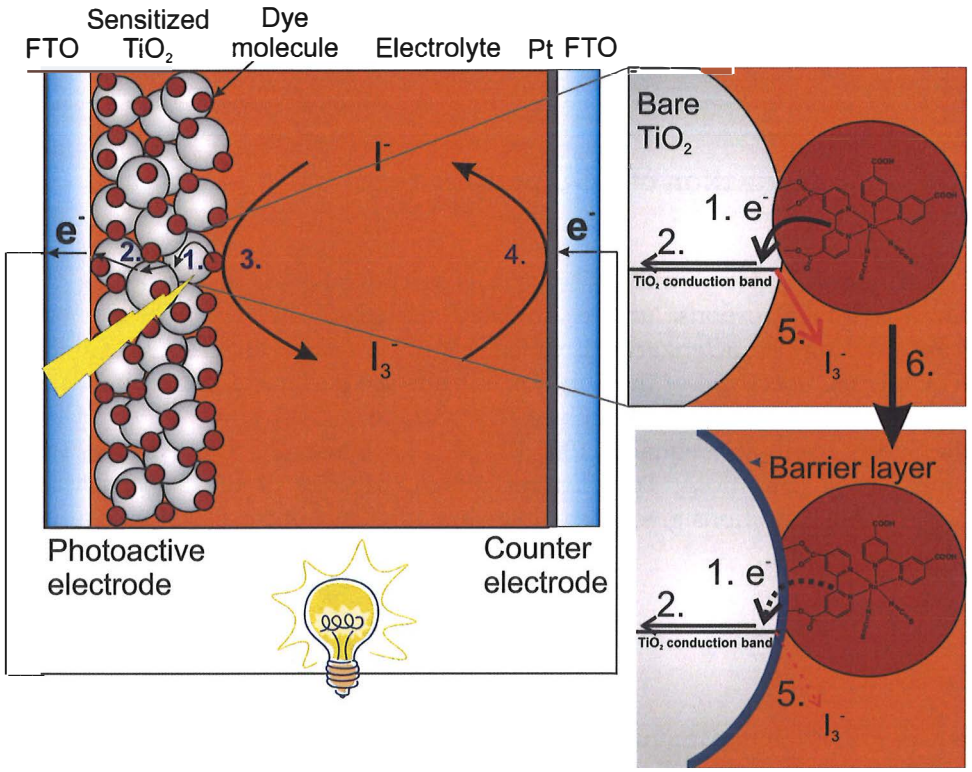

Figure 1 Components and operation principle of dye-sensitized solar cell.

In the DSC (Figure 1), the dye molecules excited by light absorption inject electrons into the conduction band (CB) of the TiO_2 nanoparticle film (1), from where electrons are transported to the external circuit (2) and the dye molecule is regenerated by the reducing agent (iodide, I^-) of the electrolyte (3). The oxidizing agent (triiodide, I_3^-) formed in the process diffuses to the counter electrode and returns to the reducing state in a platinum catalyzed reaction (4). The injected electron may be lost in a reaction with electrolyte triiodide (5). Another possible loss reaction is recombination of the injected electron with the oxidized dye. However, at sufficient iodide concentrations, it is much slower than regeneration and thus of little importance in complete DSCs.[14] Loss reactions can be suppressed by coating the surface of the semiconductor film with a protective barrier layer (6). Choice of the correct barrier material and layer thickness is crucial since the forward electron injection should be damaged as little as possible.

The DSC is a complex system: the electronic structures of TiO_2 nanoparticles and metal complex dye cover a wide range of energies. The dye-TiO_2-interactions are heterogeneous and further modified by the species in the electrolyte. The molecular level interactions in the dye-TiO_2-electrolyte interface

define many crucial processes of the DSC. In the following Sections, the dynamics of these processes—electron injection, dye regeneration and recombination of the injected electron—and their effect on overall DSC performance are described.

1.1 Characterization of DSC performance

Performance of dye-sensitized solar cells is characterized by recording their current-voltage response under simulated sunlight.[5] The standard solar spectrum used for characterization is called AM 1.5 G (AM = air mass, G = global), which is the spectrum of the Sun when it hits the surface of the Earth at a 42° angle.[15] The spectrum is normalized to make the radiant power received from the Sun per unit area equal to 1000 W/m^2. This is usually referred to as 1 sun illumination conditions. The current-voltage response of the DSC measured under these conditions gives the conversion efficiency of the DSC (or solar cells in general) as

$$\eta = \frac{P_{\max}}{P_{light}}, \tag{1}$$

where P_{max} is the maximum power output of the DSC and P_{light} = 1000 W/m^2 (or more often 100 mW/cm^2). The fill factor (FF) of the cell is the ratio between actual and theoretical maximum power outputs and can have values between 0 and less than 1:

$$FF = \frac{P_{\max}}{J_{SC}V_{OC}}, \tag{2}$$

where J_{SC} is the short circuit current density and V_{OC} is the open circuit voltage of the DSC, respectively. J_{SC} is proportional to the incident-photon-to-current efficiency (IPCE), which defines the probability that a photon of a given wavelength hitting the cell will result in an electron collected in the external circuit.[6]

$$IPCE(\lambda) = LHE(\lambda)\eta_{INJ}\eta_{CC}. \tag{3}$$

LHE is called the light-harvesting efficiency and is the probability of capturing a photon of wavelength λ by the dye molecules in the sensitized film. Injection yield η_{INJ} defines the efficiency of electron transfer from the excited dyes to the semiconductor. η_{CC} is the probability that the injected electron reaches the back contact and is collected in the external circuit.

The counter electrode equilibrates to the redox potential E_{redox} of the electrolyte. Open circuit voltage V_{OC} is therefore the difference between the Fermi level E_F of the semiconductor and the redox potential E_{redox} of the electrolyte.[5]

$$V_{OC} = \frac{E_F - E_{redox}}{e}, \tag{4}$$

where e is the elementary charge. Fermi level of a semiconductor can be written as

$$E_F = E_{CB} + k_B T \ln \frac{n_{CB}}{N_{CB}}, \tag{5}$$

where E_{CB} is the energy at the conduction band edge, k_B is the Boltzmann constant, T is temperature, and n_{CB} and N_{CB} are the densities of CB electrons and CB states, respectively. V_{OC} is thus a function of the electron concentration of the TiO_2 film. Redox potential of the electrolyte depends on the concentrations of the oxidant (I_3^-) and reductant (I^-) as

$$E_{redox} = E^{0\prime} - k_B T \ln \frac{[I_3^-]}{[I^-]}, \tag{6}$$

where $E^{0\prime}$ is the formal potential of the redox couple.

It can be shown[16] that V_{OC} depends on the flux of injected electrons Φ_{inj} and rate of recombination k_{rec} of electrons with the acceptor A in electrolyte (I_2 or I_3^-, see Section 1.3.4) as

$$V_{OC} = \frac{kT}{e} \ln\left(\frac{\Phi_{inj}}{k_{rec} n[A]}\right). \tag{7}$$

1.2 Photoactive electrode properties

The main component of the photoactive electrode of the DSC is the nanoporous semiconductor film.[5, 6] Unlike single crystal electrodes, the nanocrystalline network has a high surface area, enabling efficient sensitization via dye molecule attachment. No macroscopic electric fields exist inside the network since the small crystal size does not support significant bending of the energy bands. In addition, charges are screened by high ionic strength, liquid electrolyte penetrating the pores. Thus, the charges move by diffusion inside the semiconductor film and in the electrolyte;[17, 18] the charge separation in a DSC relies mainly on the faster kinetics of the forward electron transfer compared to loss reactions.

Titanium dioxide TiO_2 is the most commonly used semiconductor in DSCs.[5] It is stable, nontoxic, and gives the highest conversion efficiencies. Other

semiconductors used for photoelectrodes are, e.g., zinc oxide (ZnO), tin oxide (SnO_2) and niobium oxide (Nb_2O_5). Of the TiO_2 polymorphs, anatase is favored over the more stable rutile because it has a higher band gap (3.2 eV vs. 3.0 eV) and a higher conduction band energy, leading to higher DSC cell voltage. In nanoparticles, the band gap energy increases as particle size decreases.[19] For anatase TiO_2 film consisting of 13-20 nm diameter anatase particles, band gaps of 3.05-3.9 eV have been measured with photoelectron spectroscopy.[20-22] The valence band (VB) consists mainly of filled O 2p orbitals and the conduction band (CB) of empty Ti 3d orbitals. The large surface area and small crystal size make the TiO_2 particles prone to defects; therefore there is a substantial concentration of electronic states in the band gap.[17] These so-called trap states have been attributed to the presence of uncoordinated Ti^{4+} ions resulting from oxygen vacancies or lattice distortions.[23, 24] They exhibit an exponential energy distribution with shallow traps just beneath the CB edge and deep traps at ~1 eV below the CB.[21, 24, 25] Trap states may be located in the bulk, on the surface, or at grain boundaries of the TiO_2 film.

Trap states have important implications on the DSC performance: charge transport efficiency inside the TiO_2 film has been shown to depend on light intensity, suggesting a dependence on TiO_2 electron concentration.[26] This dependence has been related to electron diffusion mediated by the capture and release of electrons by the trap states (multiple trapping).[27-30] As a result, the collection time of electrons from the DSC is in the order of milliseconds to seconds.[26] At high light intensities and high electron concentration, all traps are occupied, and electrons are transported mostly via conduction band states. At lower light intensities, free trap states are available and electrons may undergo multiple trapping/releasing events during their transport. This kind of behavior is called dispersive diffusion.[28, 30]

The electronic structure of nanocrystalline TiO_2 is sensitive to preparation conditions and the environment.[21, 25] Positions of TiO_2 energy levels relative to the energy levels of the dye and the electrolyte affect the interfacial electron transfer rates, as will be discussed in more detail later. Adsorption of electrolyte species on TiO_2 surface has been shown to shift the CB energy: electron withdrawing (Lewis acidic) species of the electrolyte tend to shift the CB energy downwards (towards more positive potentials) compared to neat solvent, while electron donating (Lewis basic) species shift CB energy upwards (towards more negative potentials) (see Figure 7). Protons and cations belong to the first category as well as guanidium thiocyanate (GuSCN), which is an electrolyte additive.[20, 31-34] Other electrolyte additives, such as *tert*-butylpyridine (TBP) and N-methyl-benzimidazolium (MBI), are Lewis-basic and shift the CB energy level upwards.[35-38] In contact with a typical DSC electrolyte that contains 0.1 M Li+ and 0.5 M TBP, the CB energy has been estimated to shift upwards by ~0.5 eV.[39] Likewise, the combination of GuSCN and MBI results in an upward shift.[34]

Surface adsorption also affects the trap states: N3 dye binding and wetting the TiO_2 film with acetonitrile have been reported to decrease the band gap state density to 70% of the original value.[21] Light soaking in the presence of Na^+

and Li^+ cations lead to the formation of shallow trap states just below the CB.[38] This was found to improve the DSC current output via facilitating electron transport inside the TiO_2 film. On the other hand, slowing down recombination by adding TBP in the electrolyte has been associated to the passivation of surface trap states.[40] Metal oxide barrier layers may also shift the TiO_2 energy levels and passivate the surface states, as will be discussed later.

1.3 Interfacial electron transfer reactions at photoactive electrode

1.3.1 Marcus electron transfer theory

Interfacial electron transfer (ET) processes in the DSC have been analyzed by applying the Marcus electron transfer theory.[25, 29, 41-44] The phenomenon of electron transfer in solution can be described as follows.[45-47] The initial reactant state consists of a donor and an acceptor that are solvated by solvent molecules. Rearrangement of solvent molecules brings the system to a transition state. From this state, a turnover to the products (electron transfer from donor to acceptor) can occur if there is an electronic interaction between the donor and acceptor. The nuclei do not have time to move during the charge transfer process (Franck-Condon principle), but after the electron transfer, the geometries of the donor and acceptor and the solvent molecules rearrange according to the new charge distribution. Put in terms of free energy (Gibbs energy, FE) curves, a reactant ([D/A]) free energy curve (Figure 2) that includes the coordinates of the reactant state (position and orientation of D, A, and solvent molecules), crosses the product ($[D^+/A^-]$) FE curve that includes the same relevant coordinates for the product state (D^+, A^-, and the solvent). At the intersection, the reactant and product energy curves are split (avoided crossing). The extent of splitting is defined by the electronic coupling H^2_{AB} element. The coupling is related to the overlap and energetic matching of the donor and acceptor wavefunctions.

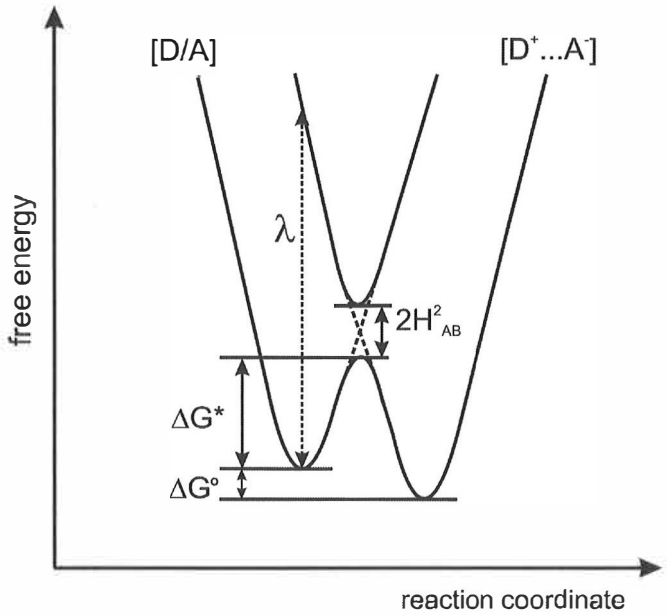

Figure 2 Free energy curves of reactant and product states and parameters relevant to Marcus electron transfer theory

If the energy splitting caused by coupling is sufficiently large (adiabatic limit), the system moves from the reactant to the product curve easily, whereas in the case of weak (nonadiabatic) coupling, it may also stay on the reactant curve. After crossing the intersection, solvent molecules reorganize and stabilize the product state. Electronic and (solvent) nuclear coupling at the intersection therefore make the transfer from one FE curve to another possible. The rate of electron transfer can be written as

$$k_{et} = A\exp\left(-\frac{\Delta G^*}{kT}\right), \tag{8}$$

where A is the pre-exponential factor and ΔG^* is the activation energy. In the adiabatic limit (strong coupling between states), the pre-exponential factor is equal to the effective frequency ν_{eff} of the system reaching the intersection of the FE curves. In the nonadiabatic limit, the pre-exponential factor is proportional to the electronic coupling H^2_{AB} of the reactant and product states:

$$A = \frac{2\pi}{\hbar}\frac{H_{AB}^2}{\sqrt{4\pi kT}}. \tag{9}$$

H^2_{AB} shows an exponential dependence on distance r between the donor and acceptor.[43]

$$H_{AB}^2 = H_0^2 \exp(-\beta r), \qquad (10)$$

where H^2_0 is the electronic coupling at $r = 0$ and β is the exponential decay constant. The activation energy depends on the free energy difference ΔG^o (driving force) between the reactants and products and on the internal and environmental reorganization energy λ. λ is defined as the change in Gibbs energy if the reactant state were to distort to the equilibrium configuration of the product state without the electron transfer.

$$\Delta G^* = \frac{(\Delta G^0 + \lambda)^2}{4\lambda} \cdot \qquad (11)$$

Therefore, in the limit of weak coupling of the donor and acceptor states, or the so-called nonadiabatic limit, the electron transfer rate can be written as

$$k_{et} = \frac{H_{AB}^2}{\sqrt{4\pi\lambda kT}} \exp\left(-\frac{(\Delta G_0 - \lambda)^2}{4\lambda kT}\right). \qquad (12)$$

In the case where the acceptor is a semiconductor, the observed rate can be written as a sum of electron transfer rates to all possible unoccupied states of the semiconductor.[46]

$$K_{ET} = \frac{2\pi}{h} \int_{-\infty}^{\infty} dE\rho(E)(1 - f(E))k_{et}, \qquad (13)$$

where $\rho(E)dE$ is the density of states of the semiconductor and $f(E)$ is the Fermi-Dirac distribution that defines the filling of the semiconductor states (with $f(E)$=0.5 when E=E_F). $\rho(E)(1- f(E))$ is therefore the probability of finding an empty state at energy E. If the semiconductor acts as a donor, the term $(1- f(E))$ is simply replaced with $f(E)$.

An important observation of the dependence of k_{et} on activation energy can be made from Equation 12: the ET rate increases with increasing driving force ΔG^o until ΔG^o becomes larger than λ. At this point, the ET rate starts to decrease with increasing driving force. This is called the Marcus inverted region.

In terms of ET processes in DSCs, the important quantities in the above equations are the coupling of the donor and acceptor states H^2_{AB} and the driving force for electron transfer ΔG^o. As already stated, the coupling depends on the overlap between the wavefunctions of the donor and acceptor states, which in turn depends on the energetic matching, symmetry, and distance of the said wavefunctions. Regarding the ET processes in DSCs, the shifting of TiO_2 CB energy discussed in the previous Section is important because it affects the energetic matching between the donors and acceptors both in the injection and recombination processes.

1.3.2 Electron injection from dye to TiO_2 conduction band

1.3.2.1 Steady-state properties of N3 and N719 dyes in solution and adsorbed to TiO_2

N3 and N719 dyes are well-suited for sensitization of TiO_2 because they exhibit a wide absorption spectrum covering most of the visible region and possess long excited state lifetimes allowing high injection yields. The absorption spectrum of N3 in ethanol shows two metal-to-ligand charge transfer (MLCT) bands in the visible region at 538 and 398 nm as well as an additional UV band at 314 nm.[12, 13] The luminescence band has a maximum located at 813 nm and a lifetime of 20 ns (in air-saturated ethanol). The absorption and emission of N719 are slightly blue-shifted due to the higher energy of the π-orbital in TBA-substituted bipyridine ligand. The excited state lifetime of N719 has also been reported to be slightly longer than that of N3.

Upon dye adsorption on nanocrystalline TiO_2 film, the carboxylate groups of the bipy-ligands form covalent bonds with the Ti^{4+} ions on the surface of the nanoparticles. There are several possible binding configurations of the dye to the surface. In the most stable configuration, two carboxylate groups from different bipy-ligands of the dye bind to the surface so that the carboxylates are as far from each other as possible.[48] The carboxylates bind via the so-called double bidentate bridging or mixed monodentate/bidentate bridging mode (Figure 3) depending on the protonation of the surface. A binding configuration via three carboxylic groups with mixed monodentate/bidentate bridging modes for N719 has also been reported.[49]

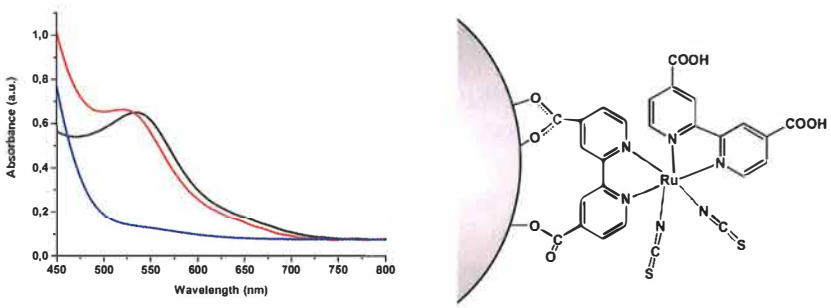

Figure 3 Left: Absorption spectrum of N3-sensitized TiO_2 film covered with 3-methoxypropionitrile (black) and with a typical DSC electrolyte (red). Blue curve is absorption spectrum of TiO_2 film covered with iodide/triiodide electrolyte. Right: Binding modes of N3 dye to the surface of TiO_2 (adapted from Ref.48).

The calculated electronic structure of N3 bound to TiO_2 shows that the dye's highest occupied molecular orbital (HOMO, ground state of the dye) consists of mixed Ru 4d and thiocyanate (SCN) orbitals and is energetically situated in the TiO_2 band gap.[50, 51] The lowest unoccupied molecular orbital (LUMO, lowest excited state of the dye) consists of dye π*-orbitals that are slightly mixed with

the unoccupied Ti (3d) states of TiO_2. The mixing of the dye and TiO_2 orbitals is enabled by their similar symmetries and enhanced by the delocalization of the bipy π^*-orbitals towards the interface via the π-orbitals of the carboxylate group used for binding.[12] This mixing causes strong coupling between the dye and TiO_2.

Upon light absorption, the transition from HOMO to LUMO shifts electron density from the Ru center to the bipy-ligands and hence the name metal-to-ligand charge transfer (MLCT) transition. The initial state is primarily singlet in character and referred to as the ^{1}MLCT state, while the relaxed excited state has triplet character and is called a ^{3}MLCT state (Figure 4). From these states, the electron is easily transferred to the unoccupied TiO_2 states.

Light absorption properties of N3 and N719 are not significantly altered upon binding to TiO_2 surface as the energies of their molecular orbitals remain similar to corresponding energies in solution.[52] This is due to a counterbalancing effect of dye deprotonation and interaction with the Ti^{4+} atoms.[49,50] In the presence of a complete DSC electrolyte, the absorption and emission of the dyes blue-shift (absorption blue-shift ~10 nm for N3). This is related to the interaction of the dye with the electrolyte cations and additives (Stark effect).[53]
Photoelectron spectroscopic measurements[21] of N3-sensitized TiO_2 films wetted with acetonitrile placed the dye HOMO state 1.75 eV below the TiO_2 conduction band edge (see Figure 7). Singlet excited state resulting from 535 nm excitation would thus be 0.17 eV higher than the TiO_2 CB level and dye LUMO (above HOMO by $E_{0\text{-}0}$ = 1.75 eV[12]) at the same energy as TiO_2 CB. Calculations are in rough agreement with the experimental results.[50,51 54] So far, detailed studies of the energy levels of the sensitized films in the presence of full DSC electrolyte have not been published.

Not many measured values of the energy levels of the dye-TiO_2 system can be found in the literature and care must be taken when evaluating energy level matching from the values measured for the separate components. For example, in acetonitrile, the flatband potential (corresponding to E_{CB}) of TiO_2 has been determined to be -1.76 V vs. NHE.[31, 32] The ground state reduction potential $E^{0'}(D/D_{ox})$ (roughly equal to the HOMO level energy) of N3 has been determined to be 1.10 V vs. NHE in acetonitrile, so the LUMO would be at -0.65 V.[12] Based on these values, no injection would take place and yet many injection studies of N3-sensitized TiO_2 films under acetonitrile have been published (see next Section). It is noted that the semiconductor energy level values reported in the literature also vary considerably (see Table 1).

1.3.2.2 Dynamics of electron injection

The charge transfer process from the excited dye to the conduction band of TiO_2—electron injection—has been widely studied and is fairly well understood when the sensitized film is in contact with solvent.[42, 55-60] Experimentally, the process can be studied with transient absorption or transient emission techniques: by monitoring the evolution of the absorption of the oxidized dye[55-72] or

of the injected electrons in TiO_2 conduction band,[41, 42, 44, 73] or by measuring the lifetimes of the ^{1}MLCT[74] or ^{3}MLCT[39, 68, 75, 76] states of the dye on TiO_2 film. Other techniques used in injection studies are, e.g., time-resolved terahertz spectroscopy.[77,78]

Dye dynamics after excitation of the lower energy MLCT band can be described to proceed as follows (Figure 4):

1) The dye singlet state undergoes ultrafast electron injection to the semiconductor in the femtosecond timescale (time constant ~50 fs).[56, 58] The strong coupling of the singlet state[49] to the unoccupied states of TiO_2 enables injection from nonthermalized singlet states even in the sub-10 fs timescale.[74] In terms of Marcus electron transfer theory, some of the nonthermalized singlet injection takes place in the adiabatic limit.
2) Intersystem crossing (ISC) from the singlet to triplet state competes effectively with the singlet state injection because of the strong spin-orbit coupling of the states. ISC proceeds with a ~70 fs time constant,[56, 58] and ~40% of the excited state population ends up in the triplet state. The states are so extensively mixed that the triplet state can be directly populated from the ground state with >620 nm excitation.[61]
3) Weak emission from the singlet state can be observed even though the injection and ISC processes are very effective. According to ultrafast fluorescence studies,[74] injection from the relaxed singlet state can still be observed 150 fs after excitation.
4) Injection from the triplet state is a heterogeneous process occurring in the picosecond timescale with time constants ranging from 1 to 100 ps.[42, 57, 60, 61, 63, 78] This behavior has been suggested to originate from the dye intramolecular dynamics[57] and heterogeneity of the interactions between the dye molecules and the semiconductor states.[42, 61, 63] It has also been claimed that the slow components are due to injection from weakly bound dye molecules or from dye aggregates.[69, 71]
5) Similarly to the singlet state, the triplet state also emits weakly.[39, 75]

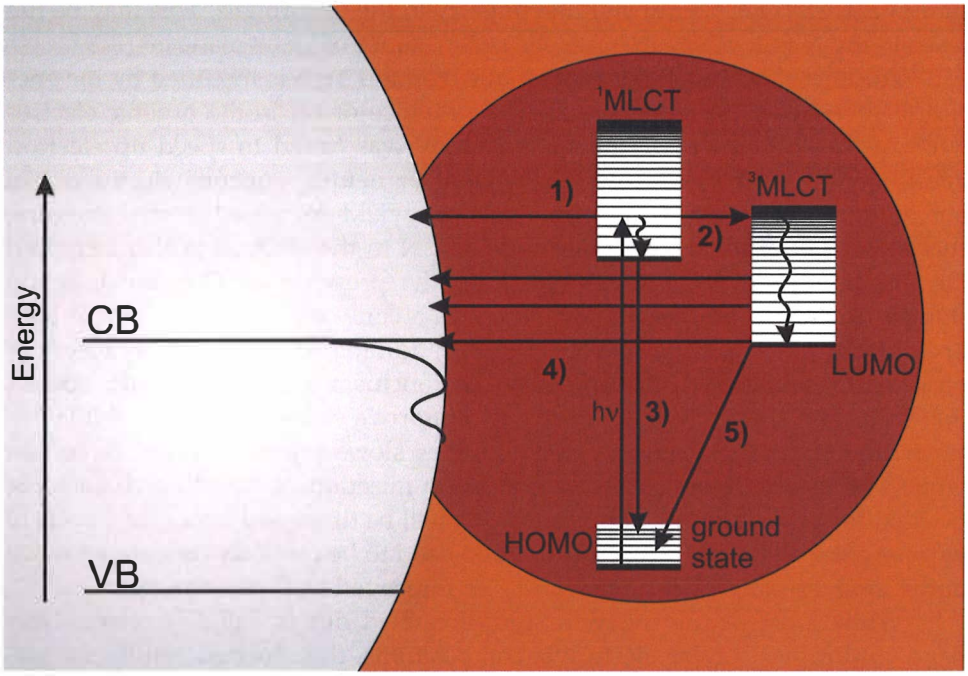

Figure 4 Simplified energy diagram of N3-sensitized TiO_2 and related electron transfer and relaxation processes (adapted from Ref. 56).

Injection from the triplet state follows Marcus electron transfer theory in the weak coupling (nonadiabatic) limit. Distance dependence of electronic coupling has been demonstrated with rhenium dyes having an increasing number of CH_2-bridging groups attached to the anchoring group.[41] Driving force dependence of injection was suggested in a study where similar dyes differing only in their excited state potential were found to inject with an increasing rate as their excited state potential moved further up from the TiO_2 CB edge.[42] The observed effect may also be due to the increase in the density of the semiconductor states at higher energies. Injection rate to different semiconductors (TiO_2, ZnO and SnO_2) was found to depend rather on the semiconductor density of states near CB than on the driving force.[41, 59] Injection was slower for SnO_2 even though it has a 0.4 eV lower CB energy than TiO_2. For ZnO, the injection was even slower despite its similar CB energy to TiO_2. These observations were interpreted in terms of a lower density of states in the vicinity of CB for SnO_2 and ZnO (effective electron masses 0.3 m_e vs. 5-10 m_e for TiO_2, Table 1) Another factor was weaker coupling between the dye and the semiconductor: As discussed in the previous Section, the N3 excited state and TiO_2 CB orbitals have similar symmetries, which enhances their coupling. The CB of SnO_2 and ZnO is formed from s- and p- instead of d-orbitals and therefore lack the favourable symmetry. Consequently, the coupling is expected to be weaker in these semiconductors. Nb_2O_5 exhibits higher CB energy than TiO_2 but has a rather high density of

states near CB ($m_e^* = 3\ m_e$) and d-symmetry in the CB orbitals. This may be the reason why Nb_2O_5 nearly matches the performance of DSCs made of TiO_2.[79]

The energetic matching between the dye and TiO_2 is modified by the species of the electrolyte (Section 1.2). The presence of Li^+ in the organic electrolyte[63] or low pH of the aqueous electrolyte[42] was found to speed up electron injection compared to neat organic solvent or neutral aqueous electrolyte. In perchlorate salt solutions, electron injection yield increased with increasing charge density of the cation.[80] Adding GuSCN to the electrolyte also increased the injection yield.[33] On the contrary, in the presence of TBP, the injection slowed down substantially.[39, 68, 71, 73, 75, 78] In a complete electrolyte where both Li^+ and TBP were present, the effect of TBP dominated—possibly because TBP replaced Li^+ from the TiO_2 surface.[36, 39] In conclusion, the Lewis-acidic species that shift the CB energy downwards also improve electron injection, while upward shift induced by Lewis-basic additives slows injection down. Note that while TBP seems detrimental to the electron injection, it has other characteristics that improve the DSC performance, as will be discussed later. The effects of various electrolyte species on the injection need to be carefully considered when optimizing the electrolyte composition for improved DSC performance.

While most of the injection studies carried out in full DSC electrolytes have used rather similar electrolyte compositions, the reported results are surprisingly dissimilar. Different studies suggest the following in the presence of full DSC electrolyte: a) the injection half-time increases 20-fold compared to the half-time in the solvent;[39, 68, 75] b) injection is not affected, but aggregation is reduced resulting in more monoexponential picosecond kinetics;[71] c) injection slows down but is still multiexponential extending from femtosecond to subnanosecond timescales.[73] This discrepancy is one of the issues tackled in this thesis.

1.3.3 Regeneration of the dye

After electron injection, the oxidized dye needs to be reduced back to its original state. This process is called regeneration of the dye, and it involves the reducing agent of the electrolyte, iodide ion (I^-) in this case. The regeneration process has been suggested to proceed via the following steps (Figure 5):[81-83]

1) Iodide ion attaches to the SCN-ligand of the dye and reduces the oxidized dye molecule. An alternative reaction would be the reduction of the oxidized dye by the iodide and the formation of an iodine atom, but this is thermodynamically forbidden;[84]

2) Another iodide ion reacts with the dye-I-complex and forms a diiodine radical (I_2^-) that is released to the electrolyte;

3) The diiodine radical may then reduce another oxidized dye molecule by forming a dye-I_2-complex;

4) Upon encountering an iodide ion, this complex dissociates and releases triiodide (I_3^-) to the electrolyte.

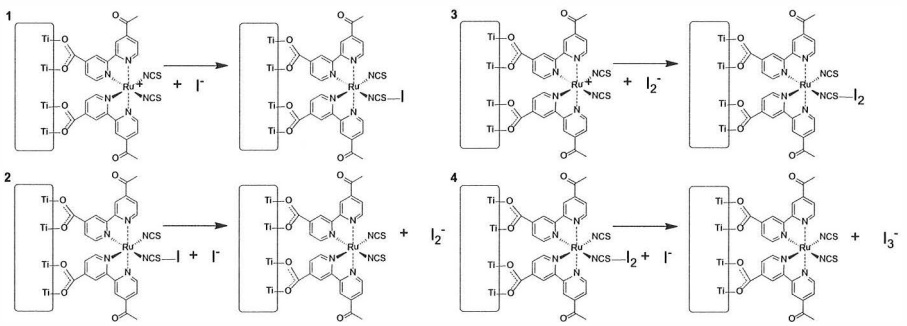

Figure 5 Regeneration of oxidized dye by iodide or diiodine

Diiodine can also undergo disproportionation by reacting with another I_2^- in the electrolyte:[85]

$$2\ I_2^- \rightarrow I_3^- + I^-. \qquad (14)$$

It has been shown by ab initio molecular dynamics simulations that I^- and I_2^- can bind to the oxidized dye molecule on TiO_2 via its SCN-ligand and form a stable, neutral complex.[81] Formation of a (D···I) complex has been observed experimentally for the dye $Ru(dcbpy)_2(CN)_2$.[86] For this dye, the positive charge is metal-centered in the oxidized state; thus, no strong LMCT absorption is observed, unlike for N3 and N719. Therefore, the absorption around 750 nm observed in the presence of LiI, but not in the presence of $LiClO_4$, can be assigned to the formation of the (D···I) complex. Formation of a stable (D···I_2) complex in N3-sensitized TiO_2 films in contact with iodine containing electrolyte has been observed both computationally and experimentally.[81] Moreover, the N3···I_2 complex has been crystallized from iodine containing methanol solution, and its crystal structure has been determined.[87]

Figure 7 shows a simplified energy scheme of N3-sensitized TiO_2-film in acetonitrile along with the redox potentials of the iodide/triiodide couple. Dye and electrolyte energy levels are depicted as Gerischer presentations. Gerischer presentation (Figure 6)[88-90] describes the energy distributions of electron accepting and donating states with the most probable energy levels of the acceptor and donor states (E^0_{ox} and E^0_{red}, respectively) displaced from the redox potential $E^{0'}$ by a reorganization energy λ'. In Gerischer's model, the reorganization energy is defined as the energy related to the reorganization of the geometry and solvation shell of the oxidized/reduced species after electron transfer. In Figure 7, the dye λ' value is assumed to be 0.3

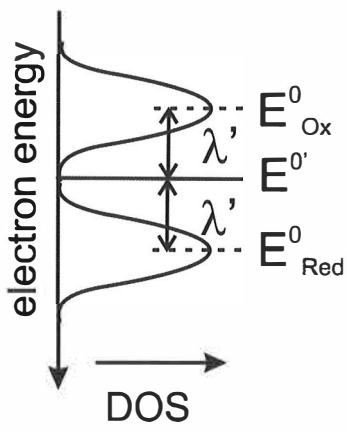

Figure 6 Gerischer presentation

eV,[83] while for I^-/I_3^-, reorganization energies of 0.4-0.7 eV have been reported.[91, 92] Also shown in the figure are the formal reduction potentials of the one-electron reactions $I_2^- + e^- \rightarrow 2\ I^-$ and $I_3^- + e^- \rightarrow I_2^- + I^-$. The redox potential of the (I_2^-/I^-) couple defines the driving force of regeneration. Furthermore, the figure reveals that a voltage loss of ~0.5 V is generated in the DSC because of I_2^- oxidation to I_3^-, which is the main drawback of the I^-/I_3^- electrolytes. Figure 7 shows that there is good energetic matching between the oxidized dye and I^-. Some overlap with the energy levels of I_2^- also exists.

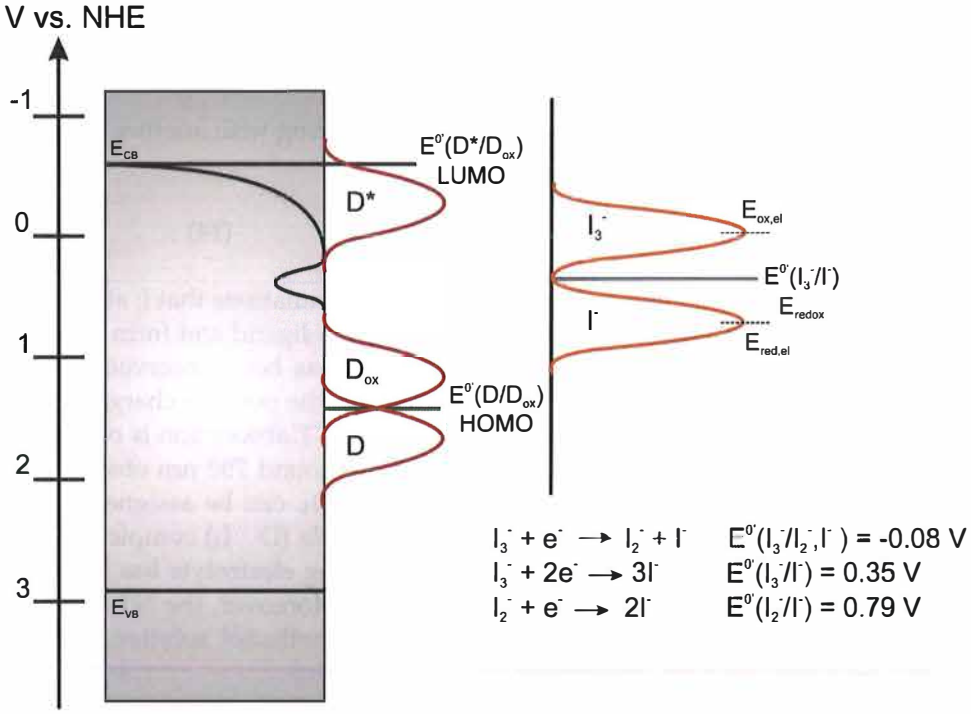

Figure 7 Simplified energy scheme of N3-sensitized TiO_2 film with redox potentials of iodide/triiodide couple in acetonitrile. Gerischer presentation was adapted from Ref. 83 and energy levels for N3-sensitized TiO_2 wetted with AcN were obtained from Refs. 12, 21. Redox potentials of iodide/triiodide couple in AcN were obtained from Ref. 93.

Steps 1 and 3 in Figure 5 therefore seem energetically favorable. Note, however, that the energy levels shown in Figure 7 were determined in neat acetonitrile (and on separate systems) and that in an actual DSC, the relative positions of energy levels may be slightly different.

The regeneration process is usually monitored with the flash-photolysis technique by following the transient absorption of the oxidized dye or that of I_2^- in the nano- to millisecond timescale.[14, 82, 86, 94-96] Another method is recording the recovery of the ground state bleach,[67, 97] but recently, it has been shown that the recovery kinetics are affected by the interaction between injected electrons and ground state dye molecules,[53] which makes the method unsuitable for re-

generation studies. In flash-photolysis experiments, the transient absorption dynamics of the N3-sensitized TiO_2 films in iodide/triiodide electrolyte at ~800 nm show a fast (half-lifetime ~1 μs) and a slow phase (0.2-0.5 s).[14] (It is noted that within these timescales, the dye excited state no longer interferes with the oxidized dye absorption). The fast phase has been assigned to the reduction of the oxidized dye and the concurrent formation of I_2^- and the slow phase to the disproportionation of I_2^- (Equation 14). The reported half-times of the fast phase vary between 100 ns and 10 μs depending on the electrolyte composition.[14, 86, 94, 96] In a complete DSC under working conditions, a ~1 μs time constant for regeneration of the dye has been reported.[82]

1.3.4 Recombination of injected electron with oxidized dye or electrolyte species

To obtain current from the DSC, the injected electron needs to be transported through the nanoparticle network and be collected to the external circuit. Due to the large surface area of the network and the slow diffusion of charges, the electron is at risk of encountering an electron acceptor at the dye-TiO_2-electrolyte interface and undergoing recombination before reaching the back contact. Such an acceptor can be a dye molecule in its oxidized state or a species of the electrolyte. The recombination processes lower the performance of the DSC. This work will focus on recombination with electrolyte species as recombination with oxidized dye is considered to be a minor loss reaction in a complete DSC.

Recombination rate shows a dependence on the electron concentration of the TiO_2 film and dispersive kinetics.[25, 29, 96, 98-100] Simulations[30] have shown that this behavior is due to the trap-limited transport of electrons to the TiO_2 surface and recombination via both CB states and surface trap states, in accordance to experimental results.[25, 91, 101] Recombination has been shown to follow the Marcus-Gerischer model, where the electron transfer from the semiconductor to the energy states of the electrolyte takes place isoenergetically (Figure 7).[91, 102, 103] At low TiO_2 electron concentration, the recombination takes place via surface trap states located on the surface of the particle. Electron transfer in this case is very slow because the electron might undergo multiple trapping events before reaching the particle surface. When electron concentration of the film increases, the traps are filled and electron transport becomes faster and less affected by the traps. Recombination also accelerates because the electrons reach the surface of the particles faster. At high electron concentrations, recombination may take place also from the conduction band states. Recombination rate at high electron concentrations is determined by the relative positions of E_{CB} and $E_{ox,el}$ (the most probable energy state of I_3^-, see Figures 6 and 7): If is $E_{ox,el}$ similar to $E_{CB,}$ the recombination rate will increase with increasing electron concentration (E_F approaching E_{CB}) because of the improved matching between the electron donating and accepting states. On the other hand, if $E_{ox,el}$ is lower than E_{CB} (as in Figure 7), recombination rate will decrease with increasing electron concentration

because the density of acceptor states decreases. In the former case, recombination of electrons will be maximized as the fast transport provides a continuous supply of electrons on the TiO_2 surface. In the latter case, the electron transport is faster than recombination at high electron concentration of the TiO_2 film— a favorable condition for good DSC performance. Electrolyte cations and additives may modify the relative positions of E_{CB} and $E_{ox,el}$: Shorter electron lifetimes (faster recombination) have been observed when the electrolyte contains small cations (Li^+)[100] compared to large cations (TBA^+, tetrabutylammonium).[92] Presence of GuSCN, TBP, or MBI increases electron lifetime.[34, 36, 37] This implies that the presence of small cations results in better alignment of E_{CB} and $E_{ox,el}$ while additives shift E_{CB} upwards, away from E_{ox}.

Another important effect of electrolyte additives on recombination is the adsorption of the additives to the TiO_2 surface. The additives are considered to block the surface from the electron acceptor, thereby impeding recombination.[12, 34, 36, 37, 40] For GuSCN the passivation effect seems to cancel the downward CB energy shift since the recombination slows down as GuSCN is added to the electrolyte.[34] It has also been suggested that TBP complexes with the uncoordinated Ti^{4+} states on the surface, thus passivating the surface trap states.[23]

There is some disagreement in the literature about the electron acceptor in the recombination reaction. Most of the papers considered in this thesis assign I_3^- as the acceptor. Recombination would then proceed[93] as $I_3^- + e^-(TiO_2) \rightarrow I_2^- + I^-$. Recently, it has been shown[104] that the recombination kinetics is actually independent of [I_3^-] but strongly dependent on [I_2]; it has been suggested that the recombination proceeds via $I_2 + e^-(TiO_2) \rightarrow I_2^-$ ($E^{0'} = +0.15$ V vs NHE). Referring to Figure 7, both mechanisms seem reasonable considering their redox potentials and energy level positions. On the other hand, the iodine concentration in the DSC is believed to be very low (~10^{-8} M). The exact mechanism of recombination thus remains obscure, but further discussion about it is beyond the scope of this thesis.

1.4 Effect of electron transfer rates on DSC performance

Summarizing the discussion of Sections 1.3.2 and 1.3.4 on the rates of injection and recombination, let us consider their effect on overall DSC performance. Referring to Equations 3 and 7 in Section 1.1, J_{SC} and V_{OC} increase when injection rate increases or recombination rate decreases, leading to higher conversion efficiency η. Achieving an increase in both J_{SC} and V_{OC} at the same time is not easy. In DSCs where electrolyte contained Li^+ and no additives, large J_{SC} and small V_{OC} were observed compared to a cell containing TBA^+.[20, 39] Li^+ caused a downward shift of E_{CB} leading to an acceleration of injection and recombination as the energetic matching of the dye-excited state and electrolyte acceptor energy levels with TiO_2 states improved (see Figure 7). Downward shift of E_{CB} improved the energetic matching of both dye excited state and electrolyte acceptor

energy levels with TiO_2 states, accelerating injection and recombination. At the same time, an additional decrease of V_{OC} was caused by the movement of E_{CB} (and therefore also E_F) towards E_{redox}. The opposite effect was observed upon addition of TBP or MBI to the electrolyte:[37, 39] J_{SC} decreased and V_{OC} increased. E_{CB} shifted upwards away from E_{redox}, diminishing the energetic matching between the dye and electrolyte energy levels with TiO_2 states and slowing down both injection and recombination. V_{OC} increase was caused both by the retardation of recombination and increased energetic separation of E_F and E_{redox}. Conversion efficiency in the latter case was better than in the former. Optimizing the DSC performance therefore requires careful balancing between the factors that accelerate/decelerate interfacial electron transfer reactions.

1.5 Improving DSC performance with metal oxide barrier layers

Prerequisites for good DSC performance are that the forward electron transfer reactions are significantly faster than the loss reactions. This is true for most of the processes depicted in Figure 1: electron injection is much faster than dye-excited state decay, and dye regeneration is much faster than recombination of the injected electrons with the oxidized dye. Only electron transport through the TiO_2 film and recombination with the electrolyte acceptor take place in the same (ms-s) timescale and compete with each other. One method for slowing down recombination relative to transport is to coat the TiO_2 surface with a thin insulating layer called a barrier layer. Most of the studied barrier layer materials are metal oxides, e.g., Al_2O_3,[22, 105-112] SiO_2,[105] MgO,[113] ZnO,[114, 115] ZrO_2,[116, 117] and Nb_2O_5,[118] but carbonates[119, 120] and titanates[116, 121] have also been investigated. This work will focus on metal oxide barriers.

1.5.1 Properties of metal oxides used in DSCs

The desired effect of the barrier layer is to impede transfer of injected electrons from TiO_2 to the electrolyte and preserve electron injection efficiency from the dye to the semiconductor. This requires careful tailoring of the material properties and thickness of the metal oxide to be used. Table 1 shows some relevant properties for the metal oxides used as photoactive electrodes or barrier layers in DSCs. As can be seen from the Table, literature reports a wide variety of conduction band energies and band gaps for metal oxides. Great care must be taken when using these values to evaluate the relative positions of the energy levels of the semiconductor with the levels of the dye and the electrolyte.

The barrier layer may affect electron transfer via several mechanisms: 1) by forming a tunneling barrier on the interface,[44, 105] 2) by shifting the TiO_2 CB energy,[105, 114] or 3) by passivating the surface trap states.[40, 107, 122, 123] The tunneling barrier may be due to increased separation between donors and acceptors or a higher potential energy region at the interface. However, the energy barrier mechanism is unlikely in the case of thin (≤ 1 nm) barrier layers because the

layers probably do not have a well-defined band structure. Instead, they are likely to modify the electronic structure of the whole TiO_2 film because the small size of the nanoparticles prevents band-bending (Section 1.2).

In previous sections, it has been pointed out that upward shifting of the TiO_2 CB energy is often favorable for the DSC performance. Table 1 presents point of zero charge (PZC) values for the metal oxides. PZC is the pH value where the semiconductor surface has zero charge.[124] Therefore, metal oxides with high PZC values are Lewis-basic and should lead to improved performance. For example, a dip-coated Al_2O_3 barrier layer was found to enhance DSC performance, while SiO_2—with a similar band gap and CB energy to Al_2O_3—was found to impair it.[105] The behavior was explained by the different PZCs of the oxides (9 for Al_2O_3 vs. 2 for SiO_2) and the consequent shifting of the TiO_2 E_{CB}. The shifts were shown as a decrease (in the case of SiO_2) or an increase (in the case of Al_2O_3) of the onset potential of dark current in DSCs with barriers compared to DSC with bare TiO_2. Upward shifting of E_{CB} by AlO_x has also been shown in reflective electron energy loss spectroscopy (REELS) measurements of TiO_2 films covered with AlO_x barrier layers.[22]

Table 1 Properties of some metal oxides

Semiconductor	TiO_2	Al_2O_3	SiO_2	Nb_2O_5	HfO_2	Ta_2O_5	Refs.
Band gap (eV)	3.05-3.9	8.45-9.9	8-9	3.4	5.7-6	3.9-4.4	20-22, 105, 117, 125-128
CB energy[a] (V vs NHE)	-0.34 -0.54 -0.66	-3.44 -4.69	-3.54 -4.48	-	-1.94	-1.24	105, 125, 129
CB electronic structure	d-orbitals of Ti^{4+}	s – and p-orbitals of Al^{3+}	s – and p-orbitals of Si^{4+}	d-orbitals of Nb^{5+}	d-orbitals of Hf^{4+}	d-orbitals of Ta^{5+}	128
m_e*[b]	5-10 m_e	-	-	3 m_e	0.1 m_e	0.3 m_e	117, 130, 131
PZC	5.8	8-9	2.1	4.1	7.1-7.6	5-5.3	105, 124

[a]CB energy is equal to electron affinity of semiconductor. [b]Density of conduction band states is proportional to effective electron mass m_e*.

Note that Lewis-basic metal oxides will adsorb more dye than Lewis-acidic ones. For example, an N3-sensitized TiO_2 film with Al_2O_3 barrier had 40% higher optical density than films with no barrier when sensitized to saturation with N3.[105] The amount of dye in the film with SiO_2 barrier was only half of that of the bare film. Ignorance of different dye binding efficiencies on applied barrier layers may lead to erroneous interpretations of the function of the barriers in DSCs.

When barrier layers are prepared with just a few atomic layer deposition cycles (see Section 2.1.2), so called submonolayers are formed on the TiO_2 surface. Coverage depends on the size of the metal alkyl used in the deposition and on the number of ALD cycles applied. Dye molecules may bind to the

submonolayer or on the exposed TiO_2 surface—the binding distribution between different sites depending on the size of the holes in the deposited layer. The effect of the submonolayers on electron transfer can be understood as a tunnel barrier effect caused by the increased physical separation of the dye molecules from the TiO_2 surface or by shifting the TiO_2 CB due to the coating. The increased distance affects the electronic coupling between the dye and the surface. Here, the symmetry of the unoccupied metal orbitals of the metal hydroxide groups forming the submonolayer may be of relevance. The binding orbitals of the dye (bipy) and TiO_2 have d-symmetry, so their electronic coupling is expected to be less affected by metal oxides whose CB has similar symmetry, e.g., HfO_2, Ta_2O_5, and Nb_2O_5 (see also Section 1.3.2).

2 EXPERIMENTAL METHODS

This chapter will describe the preparation and characterization of the samples: the TiO_2 films with and without metal oxide barrier layers and the DSCs assembled from these films. The basics of atomic layer deposition will be presented as well as the methods used to study the electron transfer processes and the overall DSC performance.

2.1 Sample preparation

Spectroscopic measurements were carried out on dye-sensitized TiO_2 films covered with the solvent 3-methoxypropionitrile (MPN) or with the iodide/triiodide (I^-/I_3^-) DSC electrolyte in same solvent. For EIS measurements and IV-characterization, a number of similarly prepared DSCs were assembled. Metal oxide barrier layers were grown on part of the TiO_2 films by atomic layer deposition.

Nanoparticle films were prepared by the doctor blading method on infrared transparent calcium fluoride (CaF_2) windows or on FTO coated glass substrates. For TiO_2 films, commercial TiO_2 colloid or "paste" from Solaronix was used (Ti-Nanoxide HT or Ti-Nanoxide T). Al_2O_3, HfO_2, and Ta_2O_5 films used as references were prepared from homemade colloids by a previously reported method.[12] The Al_2O_3 colloid was prepared from commercially available particles (Degussa), while HfO_2 and Ta_2O_5 particles were synthesized according to Ref. 132.

In the doctor blading method, the colloid is spread on the substrate with a glass rod. Scotch tape is used to define the area and the wet thickness of the film. After doctor blading, the films were sintered at 450 °C for 30 min to fuse the nanoparticles together and burn off the organic additives and solvent of the colloid. The resulting TiO_2 films were highly transparent, while the Al_2O_3 films were slightly opaque. The thickness of the films was chosen to be 2–3 μm to keep light scattering at a minimum during the time-resolved spectroscopic

measurements. Some of the prepared TiO_2 films were coated with a metal oxide barrier layer by atomic layer deposition (see next Section).

Dye-sensitization was carried out by immersing the films in 0.3 mM N3 (Dyesol) or N719 (Solaronix) ethanolic solution. The sensitization times were varied to obtain matched optical densities for the films used in the barrier layer studies. Exposure of the sensitized films to ambient air was minimized.

2.1.1 Sample preparation for spectroscopic, EIS- and IV-measurements

The photoactive electrodes of the DSCs were used in spectroscopic studies. For the samples of Paper II, the solvent was injected in the space between the two glass substrates separated by a Surlyn spacer and then clipped together. In Paper I, the CaF_2 window with sensitized film was assembled into a flow-type cell[133] with another CaF_2 window and a Surlyn frame. The use of a flow cell allowed minimizing the exposure of the dye to the ambient atmosphere during liquid exchange. Typically, the measurements were first carried out in solution and then in the electrolyte. FTO glasses could also be glued together with the Surlyn spacer frame and fill the space between the electrodes with a suitable liquid in a flow cell. The sample was then removed from the cell for measurements where the bulky flow cell could have obstructed the signal.

For EIS- and IV-measurements, functioning DSC cells had to be prepared. Counter electrodes for DSCs were prepared by spray deposition and thermal decomposition of hexachloroplatinate (H_2PtCl_6) solution on clean FTO coated glass pieces. Sandwich cells were then made from the photoactive and counter electrodes by bonding them together with a Surlyn foil frame (thickness 25 μm).

Two similar electrolyte compositions were used in the experiments reported here:

1) 0.5 M 3-hexyl-1-methyl-imidazolium iodide (HMII, synthesized according to Ref. 134) 0.1 M anhydrous lithium iodide (LiI), 0.05 M I_2, and 0.3 M *tert*-butylpyridine (TBP) in 3-methoxypropinitrile (MPN). This electrolyte was used in Paper III and in the first set of HfO_x samples;

2) Similar to electrolyte 1 but HMII was replaced by 0.6 M 3-propyl-1-methyl-imidazolium iodide (PMII) and the concentration of TBP was increased to 0.5 M. The latter composition has been reported to yield better DSC performance than the former.[39] Also, the electrolyte solvent was dried by distillation for electrolyte 2; otherwise, molecular sieves were used. Electrolyte 2 was used in Paper I, in the second HfO_x sample set, and in the TaO_x sample set.

The electrolyte was introduced to the cell in a vacuum chamber via a pipette tip placed on a hole in the counter electrode. Air in the space between the electrodes was removed in a ~1 mbar vacuum and replaced with the electrolyte when normal atmosphere was restored. The hole in the counter electrode was then sealed with Surlyn.

2.1.2 Atomic layer deposition of barrier layers

Traditionally, barrier layers have been prepared by the sol-gel dip-coating method.[44, 105, 107, 114, 135] It involves dipping the TiO_2 film in a metal alkoxide solution followed by heating and consequent formation of the respective metal oxide. Layer thickness can be increased by repeated dippings. While the method is quite simple, it suffers from poor penetration of the liquid precursors into the pores of the film,[44] and rather thick (~1 nm) layers are formed already in a single dipping cycle.[105] Lately, atomic layer deposition has become the method of choice for barrier layer preparation.[22, 40, 109, 111, 112, 122, 123, 136, 137]

Atomic layer deposition (ALD) is a chemical vapour deposition method where gaseous reagents react with a solid surface in a step-wise and self-terminating manner.[138] In this work, ALD was employed to coat the nanoporous TiO_2 film with metal oxide barrier layers. The advantage of ALD compared to the sol-gel dip-coating method[135] more traditionally used for barrier layer preparation is the good penetration of the ALD layers into the nanopores of TiO_2 all the way through the film thickness (gaseous vs. liquid reagents) and superior controllability of the deposited layer thickness. The latter is based on the surface-saturating nature of the ALD reactions.

As an example of an ALD process, let us consider the deposition of Al_2O_3 on TiO_2 by using trimethylaluminum (TMA) and water as precursors.[138] After the gaseous TMA is introduced into the reaction chamber, it will react with the hydroxyl-groups on the TiO_2 surface through ligand exchange. Aluminum binds to the oxygen atom of the OH-group, and a methyl group reacts with hydrogen releasing methane in the gas phase. TMA will react with all available OH-groups forming a molecular monolayer of oxygen-bound $Al(CH_3)_2$-groups on the surface. Then, the reaction stops (Figure 8A). The chamber is purged with nitrogen and evacuated to remove the residual TMA. In the second step of the ALD cycle, water is introduced to the chamber. Water will react with the bound $Al(CH_3)_2$-groups, replacing the methyl groups with OH-groups and forming gaseous methane (Figure 8B). After the chamber has been purged and evacuated again, the ALD cycle is complete. In the next cycle, the TMA will react with the $Al(OH)_2$-groups formed in the previous cycle, and the cycles are repeated until the desired layer thickness is reached. In principle, the same amount of material is deposited in each cycle so that just by varying the number of deposition cycles, different layer thicknesses can be obtained in a reproducible manner with atomic layer precision. As the material is added atomic layer by atomic layer, smooth and continuous films can be made with precisely defined layer thicknesses up to about 100 nm.

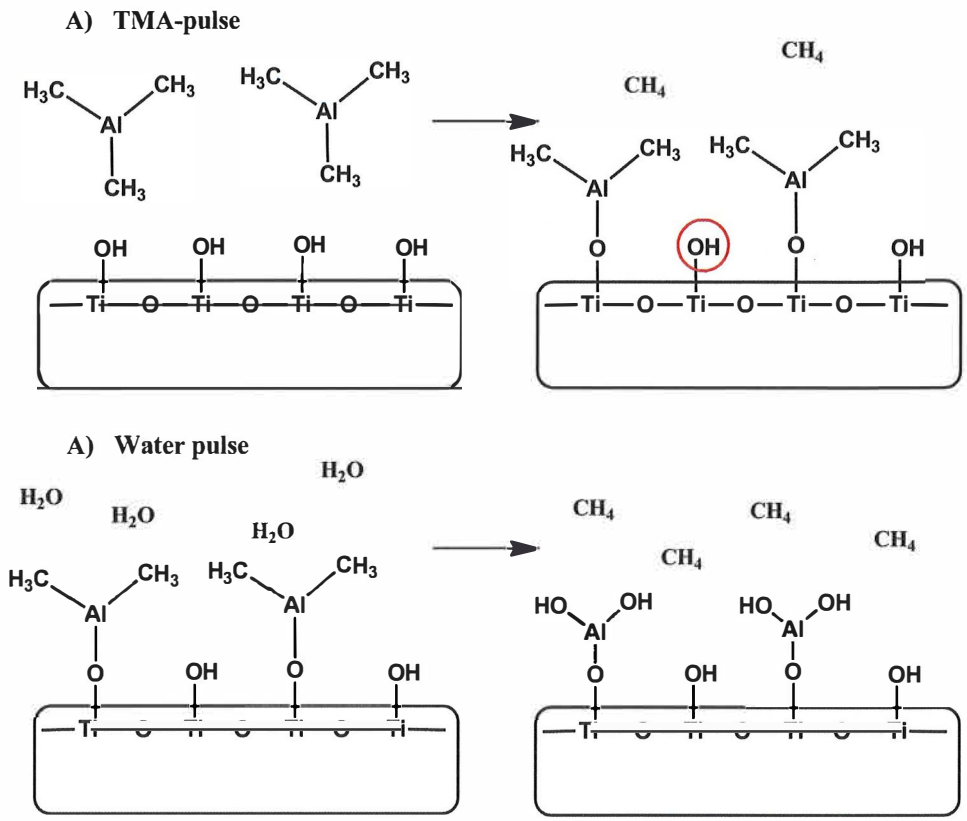

Figure 8 Simplified binding scheme of TMA-H_2O -process

The growth-per-cycle is defined as the amount of material deposited during each cycle per unit area (nm^{-2}). However, in the literature, GPC is often given in units of nm/cycle referring to the thickness increment per cycle of the deposited material (0.1 nm/cycle for the TMA-H_2O process). This practice is somewhat problematic, since the thickness increment per cycle, Δh, is actually an average value determined by measuring the thickness of a bulk-like layer and dividing it with the number of cycles. The GPC is roughly the same for each individual cycle, but the Δh is not since it depends on the density of the material, which is different in the interfacial regions and in the bulk.

The benefits of ALD become evident when ten or more cycles are used for layer deposition. For thinner layers, interfacial and molecular level effects affect the growth of the film. This was manifested in the layers used in this work, where only 1–5 ALD cycles were used for the deposition of Al_2O_3. First of all, during one cycle, a monolayer is formed by the precursors (TMA), not by the product (Al_2O_3). This means that though the precursors (TMA molecules) pack tightly on the surface, some binding sites are unavailable (circled in Figure 8) due to steric hindrance between the CH_3-sidegroups. When the side groups are removed, these sites become open. In other words, the deposited layer is not continuous but contains holes. If the deposition process continues, the TMA

molecules of the next cycle can now in principle bind to the bare surface or to the layer deposited in the previous cycle. This will make the surface rough at the atomistic scale and lead to non-constant Δh, as the composition of the surface varies from cycle to cycle.

In this work, barrier layers consisting of three different metal oxides were prepared by atomic layer deposition of respective precursors on the nanoporous TiO_2 films. The studied metal oxides were aluminium oxide, hafnium oxide, and tantalum oxide. As the layers were very thin (≤ 1 nm) and their stoichiometry could not be precisely defined, the materials are referred to as AlO_x, HfO_x, and TaO_x. Metal alkyls and water were used as precursors in the ALD process. Figure 9 shows the structures of the metal alkyls used.

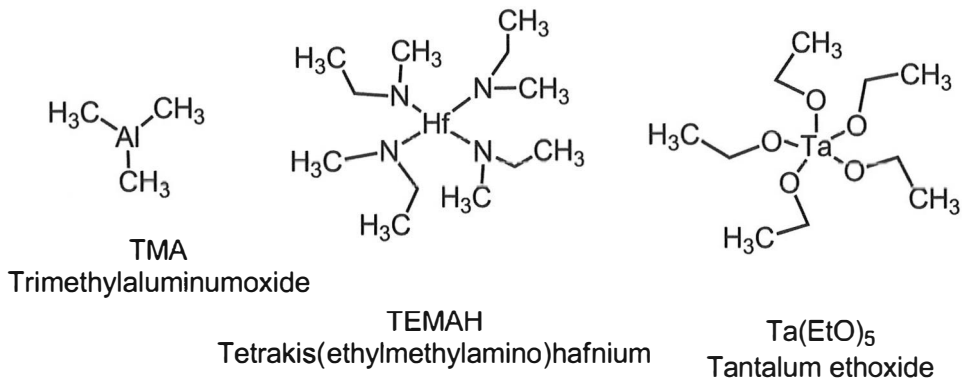

Figure 9 Molecular structures of metal alkyl precursors used in ALD of respective metal oxides

As already mentioned, the studied AlO_x barrier layers were deposited with 1–5 ALD cycles. For HfO_x, preliminary studies were conducted with layers grown with 1–4 ALD cycles, and later, thicker layers grown with 12 cycles were also included. According to the reported GPC value of the TEMAH-water process, 12 cycles should result in a ~1 nm thickness of the deposited layer (Δh =0.09 nm/cycle).[139] Similarly, for TaOx barriers, the thickest layer studied was grown with 28 cycles, which was supposed to result in a 1 nm thick coating (Δh =0.04 nm/cycle[140]).

2.1.3 Characterization of barrier layers

The coverage of ALD grown layers in the pores of the TiO_2 films was studied with ion-beam techniques. Rutherford back-scattering spectrometry (RBS) was employed to ensure that the metal oxide layer had penetrated throughout the thickness of the film. In RBS, the sample is bombarded with He ions, and the elements present in the sample identified from the energy losses of the back-scattered probing ions.[141] The depth profiles of the respective elements can then be calculated by means of scattering kinematics and stopping powers. The drawback of the method is that it is relatively insensitive to low-atomic mass

elements and for elements lighter than the substrate. RBS is therefore well-suited for the analysis of hafnium and tantalum oxide layers on TiO_2 but not so much for aluminium oxide. Thus, the coverage of AlO_x on the TiO_2 surface was studied also with Time-of Flight Elastic Recoil Detection Analysis (ToF-ERDA). In ToF-ERDA, the sample is bombarded with heavy ions, such as Br^+ and forward-scattered sample atoms are detected. The scattered atoms pass two timing gates on their way to the detector, allowing determination of both energy and mass of the atoms. ToF-ERDA measurements were performed on a flat ALD grown anatase surface coated with 1–5 ALD cycles of AlO_x. The area density of aluminium was determined and compared with the densities obtained from DFT calculations (Section 3.2.1).

Ultraviolet photoelectron spectroscopy (UPS) was used to study the effect of the barrier layers on the energy levels of the TiO_2 film. In UPS, ultraviolet photons hitting the sample release electrons from the outermost valence orbitals.[142, 143] The electrons may suffer from collisions upon exiting the sample; therefore two kinds of electrons arrive at the detector: 1) primary electrons that did not undergo collisions and 2) secondary electrons that lost varying amounts of energy in inelastic collisions. The kinetic energy of the primary photoelectrons is $E_{kin} = h\upsilon - E_b - \Phi$, i.e., the energy of the incident photons subtracted by the binding energy E_b of the electron and the work function Φ of the material. The binding energy of the photoelectrons corresponds to the energy of the orbital from which they originated (Koopmans' theorem). Primary electrons allow the determination of the binding energy of the most loosely bound electrons, i.e., valence band maximum of the semiconductors. The slowest secondary electrons lose all of their kinetic energy in collisions and can barely overcome the work function. Therefore, their binding energy is equal to the difference between the photon energy and the work function of the sample $E_b = h\upsilon - \Phi$.

The UPS measurements were carried out on similar 2 μm thick TiO_2 films as used in the actual DSCs. The studied coatings were prepared with 1–10 ALD cycles. For TaO_x, coating deposited with 28 cycles was also studied. He(I) line (21.22 eV) was used as the photon source, and the samples were stored in ambient conditions prior to measurements to resemble the films used to prepare the actual DSCs as closely as possible.

2.2 Transient absorption spectroscopy

In transient absorption (TA) spectroscopy,[144, 145] a short-lived species is generated by optical excitation and its lifetime recorded by following the time evolution of its absorption. It is a convenient method to study reaction kinetics in cases where the reactant, product, or both absorb light. The optical excitation is provided by a laser pump pulse, and a second pulse is used to probe the induced change in absorption. Hence, the method is also called pump-probe spectroscopy.

Time evolution of absorption is described by the time-dependent Lambert-Beer law:

$$A[OD](\lambda,\Delta t) = \log\frac{I_0(\lambda)}{I(\lambda,\Delta t)} = \sum_i^n \varepsilon_{i,\lambda}\, N_i(\Delta t) l\,, \qquad (15)$$

denoting that the observed absorbance (optical density, OD) at wavelength λ and at time Δt after excitation is the logarithm of the ratio of the intensities of the incident and transmitted light. This is equal to the sum of the absorbances of all species i that absorb at wavelength λ. Absorbance of species i is equal to the product of molar absorption coefficient $\varepsilon_{i,\lambda}$ and population N_i of the species at time Δt and optical path l.

Time resolution of the TA experiment is defined by the instrument used. In nano- to millisecond TA spectroscopy (flash-photolysis), time resolution is limited by the response time of the detector to the nanosecond timescale. For ultrafast TA spectroscopy, where events in the femto- to picosecond timescale domain are explored, no detecting system is fast enough to observe the pulse profiles directly, and the absorption change of the sample has to be determined separately for each time delay Δt. This is achieved in an optical delay line that can be used to produce a controllable delay between the probe pulse with respect to the pump pulse (Figure 10). Hence, the time resolution of the experiment is limited only by the duration of the laser pulses. The instrument response function (IRF) can be determined by measuring the cross-correlation signal of the pump and probe pulses; the FWHM of the time profile of the cross-correlation signal is the time resolution of the experiment.

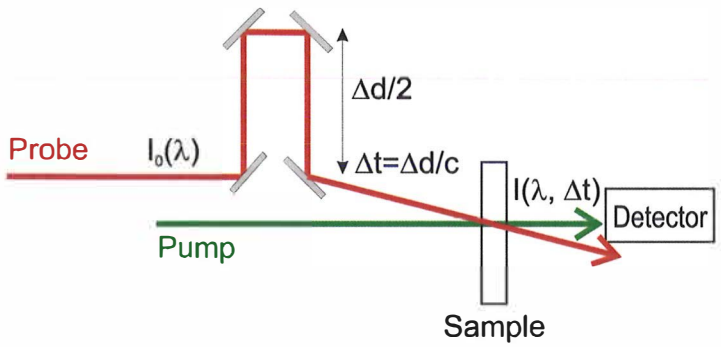

Figure 10 Simplified scheme of pump-probe method.

The signal is recorded as differential absorption

$$A[OD](\lambda,\Delta t) = \log\frac{I_0(\lambda)}{I(\lambda,\Delta t)}_{excitation} - \log\frac{I_0(\lambda)}{I(\lambda,\Delta t)}_{no\ excitation}\,, \qquad (16)$$

i.e., as the difference in optical density at the probe wavelength without excitation and after excitation by the pump pulse. The time evolution of the differential absorption signal reveals the kinetics of the probed process.

Electron transfer kinetics in DSCs is in general very nonexponential and described with a distribution of rate constants rather than a single constant. In this work, multiexponential decay law was used to analyze the measured kinetics.

$$\Delta A(t,\lambda) = \sum_{i}^{n} A_i(\lambda)\exp(-\Delta t/\tau_i). \qquad (17)$$

The multiexponential decay is a sum of n exponential functions with characteristic amplitudes and time constants. The law assumes that there are n states from which the electron transfer can take place and each of these channels has a characteristic rate. Another decay law often used to analyze electron transfer kinetics is the stretched exponential decay law where the heterogeneity of the system is taken into account via so-called stretch parameter β. In data analysis, the instrument response function is convoluted with the chosen decay law to obtain a model function. The model function describes the response of the system to the instrument response function. The parameters of the model function (amplitudes, time constants) are then obtained through non-linear least-squares fit to the experimental data.

In DSCs, TA spectroscopy can be used to study the kinetics of electron injection, dye regeneration, and recombination of the injected electron with the oxidized dye. In this work, the first two processes were examined with ultrafast TA spectroscopy. Electron injection kinetics can be revealed by monitoring the evolution of the absorption of the oxidized dye[55-72] or of the injected electrons in the TiO_2 conduction band.[41, 42, 44, 73] The former approach is the most commonly used technique for electron injection studies in DSCs.

After excitation at the lower energy MLCT band of the dye and consequent electron injection, the positive charge localizes on the SCN ligand of the oxidized dye,[43, 146] giving rise to a strong ligand-to-metal charge transfer (LMCT) absorption with a maximum around 800–850 nm.[55] However, other species, such as the dye-excited state (absorption maximum at 720 nm) and TiO_2 conduction band electrons also absorb in the near-infrared region, complicating the interpretation of the observed kinetics.[55] Probing wavelength must therefore be selected carefully:[60] The excited state of N3 has an isobestic point at 860 nm and for N719, it is blue-shifted to 810 nm. Very little excited state dynamics is observed at the isobestic point, making 860 and 810 nm ideal for monitoring the formation rate of the oxidized N3 and N719 dyes, respectively, which absorb in these spectral regions. TiO_2 electron absorption in the near-infrared is weak compared to oxidized or excited state dye absorption and can be neglected.[55] The absorption coefficient of the oxidized dye is larger than that of the dye-excited state, so the dynamics recorded in the near-infrared will ultimately reflect the formation of the oxidized dye. However, recording transient absorp-

tion of a noninjecting sample, such as sensitized Al_2O_3 or ZrO_2, is necessary to determine the excited state contribution to the dynamics.

Another way of monitoring injection is to probe the arrival of injected electrons in the semiconductor. Conduction band electrons of TiO_2 exhibit a broad absorption band in the mid-infrared (mid-IR) region extending from 3000 to 900 cm^{-1}.[147, 148] N3 and N719 dyes exhibit several vibrational peaks in this spectral region, but above 2000 cm^{-1}, there is a window where vibrational bands do not interfere with electron absorption.[73, 149] In this work, electron absorption was probed at 1960 cm^{-1}. Since only CB electrons contribute to the absorption in this wavelength region, the observed kinetics may be influenced only by the fast (~100 fs) trapping of the electrons into TiO_2.[150]

In this work, the sensitized TiO_2 films were studied by exciting at the lower energy MLCT band and probing in the near-infrared or in the mid-infrared. The excitation pulses were generated via noncollinear parametric amplification (NOPA) of white light continuum (generated in a sapphire crystal). The pulses were compressed with a prism pair. In Paper I, white-light continuum was used for probing, and suitable 8 nm band widths were selected for monitoring with a monochromator and recorded with a pair of diodes. Otherwise, the 860 nm probe pulses were generated with NOPA and compressed with a prism pair. The mid-infrafred probing pulses were generated in a home-built, double-pass optical parametric amplifier and by frequency difference mixing in a type II $AgGaS_2$ crystal. Time resolutions of the experiments were in the range of 200–250 fs and 65–90 fs in the experiments where compressed pulses could be used.

2.3 Transient emission spectroscopy

Transient emission spectroscopy can be used to record the luminescent lifetimes of molecules. In this work, time-correlated single photon counting (TCSPC) was used to determine excite state lifetimes and injection rates of N3 and N719 dyes on TiO_2 and Al_2O_3 films. Although the emission originates from the dye excited state and not the oxidized dye, the observed lifetime is proportional to the time constant of injection. The observed lifetime is the inverse of the sum of the rates of all the processes that consume the excited state population. In the case of sensitized TiO_2 films, the observed lifetime can be written as

$$\tau_{obs} = \frac{1}{k_r + k_{nr} + k_{inj}} \approx \frac{1}{k_{inj}} = \tau_{inj}, \qquad (18)$$

where k_r is the rate of radiative decay (luminescence), k_{nr} is the rate of nonradiative decay, and k_{inj} is the rate of electron injection. As $k_{inj} >> k_r, k_{nr}$, the observed lifetime is effectively the average lifetime of injection τ_{inj}.

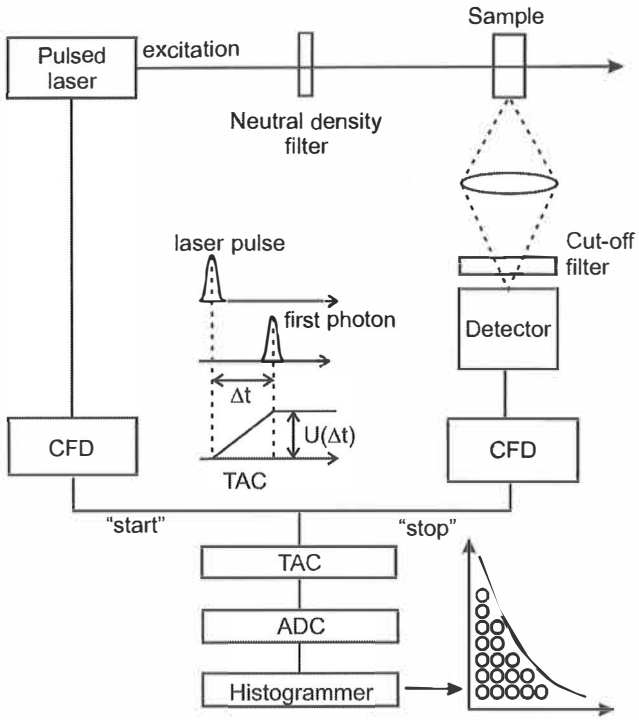

Figure 11 TCSPC operation principle. Adapted from Refs. 151, 152.

In TCSPC, fluorescent decay is recorded as separate events,[151] allowing time resolution of events taking place in the timescale of hundreds of picoseconds to milliseconds. The time profile of the emission is constructed by electronically measuring the time delay between the exciting laser pulse and an emitted photon arriving at the detector. The cycle of excitation–detection of the arrival of the first photon is repeated, and a histogram of the arrival times of the photons to the detector is formed. The emission decay profile is obtained from the histogram.

In more detail, a laser pulse excites the sample, which starts to emit. A constant-fraction discriminator (CFD) is used to time the arrival of the pulse at the sample and to send a 'start' signal that induces the generation of a linear voltage ramp in a time-to-amplitude converter (TAC). A second CFD times the arrival of the first emitted photon at the detector and sends a 'stop' signal to the TAC. The accumulated voltage is proportional to the time delay between the excitation pulse and the emitted photon. An analog-to-digital converter (ADC) converts this information to a numerical value that is stored as a single event corresponding to the measured time delay in a histogram. Only the first arriving photon can be detected due to the dead time of the electronics, so the number of incoming photons must be kept low (less than 1 photon/100 laser pulses). If many photons arrive per cycle, the histogram is distorted at early times.

The instrument response function (IRF) depends on the laser pulse duration and the characteristics of the detector and timing electronics. The time profile of IRF can be determined with the help of a suitable scattering sample, such as milk or lens paper. The data analysis is carried out in a similar way as in transient absorption spectroscopy.

In Paper I, TCSPC measurements were carried out on N3- and N719-sensitized TiO_2 and Al_2O_3 films in solvent and in a typical DSC electrolyte. The optical densities of the films were matched as closely as possible, and photons were collected for fixed time periods to ensure similar number of absorbed photons in all samples. The excitation wavelength was 483 nm, and emission was collected at wavelengths longer than 670 nm. For Al_2O_3 samples, the decay was fitted with a sum of two exponentials convoluted with the experimental IRF. For TiO_2 samples, three exponentials were used in the fit.

2.4 Current-voltage response and electrochemical impedance spectroscopy

The DSCs were characterized by measuring their current-voltage (IV) response in dark and under 1 sun illumination conditions. Illumination was calibrated by setting the light source (Solux halogen lamp) to an appropriate distance from a calibrated silicon reference cell (PV Measurements, Inc.) so that the current output of the cell matched to 1 sun illumination. IV responses of the DSCs were recorded by sweeping a bias voltage from -0.2 to 0.7 V and back in 10 mV steps. IV behavior of DSCs exhibits hysteresis related to the slow, trap-mediated transport of electrons, making the slow scanning of the voltage in both directions necessary. Reported IV responses are the averages of the two scans. Current-voltage response without illumination was recorded to obtain information about how easily the TiO_2 electrons can be transferred to the electrolyte. The dark current is not equivalent to the recombination current because the charge distributions are different under illumination and in the dark. However, changes in the onset potential of the dark current can be used to estimate changes in recombination rate induced by shifts of the TiO_2 CB energy.[116]

Electrochemical impedance spectroscopy (EIS) was carried out under illumination to determine the effect of barrier layers on recombination in the DSCs. Electrochemical impedance is measured by applying a small alternating voltage signal to the cell in a range of frequencies and recording the impedance (output current and voltage of the cell and their phases, respectively) at each frequency. The EIS response of a DSC depends heavily on the conductive state of TiO_2.[37] Therefore, the DSC is usually set to an operation point by applying a DC bias potential to the cell and recording the EIS response at several operation points. The advantage of EIS is that it allows studying each DSC component separately, as their time constants are different; therefore their impedance responses appear at different frequencies. By plotting the (negative) imaginary

component of the impedance as a function of the real component, a Nyquist plot is obtained. In a Nyquist plot, the different cell components show as semi-arcs that become more distinctive as the bias potential increases (Figure 13). With the help of a suitable equivalent circuit (Figure 12), charge transfer properties of the cell components can be extracted from the Nyquist plot.

Figure 12A shows the complete equivalent circuit of a DSC with the following components:[37, 153]

- Series resistance R_s describing FTO sheet resistance, contacts, etc.
- Transport resistance R_T at the TiO_2-electrolyte interface (= $r_t d$; r_t is the resistivity of the film, and d is the film thickness)
- Charge-transfer resistance R_{CT} at the TiO_2-electrolyte interface (= r_c/d)
- Constant phase element describing the chemical capacitance C_μ (=c_μ/d) of the TiO_2 film
- Charge-transfer resistance R_{CE} and the capacitance CPE_{CE} of the counter electrode
- Charge-transfer resistance R_{CO} and the capacitance CPE_{CO} of the substrate-TiO_2 interface
- Charge-transfer resistance R_{SU} and the capacitance CPE_{SU} of the substrate-electrolyte interface
- Diffusion resistance Z_d of the electrolyte
- Series inductance L describing the inductance in the wires

Constant phase elements (CPEs) are used to describe the interfacial capacitive elements of the DSCs instead of capacitors because of the heterogeneous (porous) nature of the interfaces. The impedance of a CPE can be written as $Z_{CPE} = [C\,(i\omega)^{\beta}]^{-1}$, where parameter β defines the angle of the impedance curve in the complex plane. β can have values from -1 to 1. If β =1, the CPE is a pure capacitor, and the Nyquist plot shows a semicircle for the parallel R-CPE combination. When β decreases, the shape of the semicircle becomes 'depressed'. The capacitive elements of the DSCs correspond to double layer CPE except for the CPE_{CT} element at the TiO_2-electrolyte interface (Figure 12). The impedance of this element can be written as $Z_{CPE\_CT} = [C_\mu\,(i\omega)^{\beta}]^{-1}$, where C_μ is the chemical capacitance of the TiO_2 film that describes the change of electron density as a function of the Fermi level.[154, 155]

$$C_\mu = e^2 \frac{\partial n}{\partial E_F} = \frac{e^2}{kT} \exp\left[\frac{\alpha}{kT}\left(E_F - E_{CB}\right)\right], \qquad (19)$$

where n is the density of free and trapped electrons in the film and α is a constant related to the distribution of trap states. Charge-transfer resistance can be written as: [46, 154]

$$R_{CT} = R_0 \exp\left[-\frac{\beta'}{kT}\left(E_F - E_{redox}\right)\right], \qquad (20)$$

where R_0 is a constant inversely related to the recombination rate[103] and β' is the transfer coefficient (typically 0.5-0.7).[102] Both C_μ and R_{CT} therefore exhibit an exponential dependence on voltage and on electron concentration of the TiO_2 film.

The diffusion impedance Z_d of the electrolyte corresponds to finite-length Warburg (FLW) impedance, which describes the diffusion of a particle in a finite-length region of length L'.[156] The impedance of this element can be written as

$$Z_d(\omega) = R_d \frac{\tanh(i\omega s)^\varphi}{(i\omega s)^\varphi}, \qquad (21)$$

where R_d is the diffusion resistance in the limit of Z_d ($\omega \rightarrow 0$) and $s = L'^2/D'$. ω is radial frequency, D' is the diffusion constant of I_3^-, and L' is taken as half of the distance between the electrodes. For the finite-length Warburg impedance, the exponent in Equation 21 is $\varphi = 0.5$. In this work, a generalized FLW element Z_d with $0 < \varphi < 1$ was used in the fitting. The obtained φ values were close to 0.6 in Paper III. In the data analysis of other sample sets, the diffusion impedance was left out since it was not expected to be affected by the barrier layers.

The conductive state of the photoactive electrode greatly affects the shape of the Nyquist plot and the number of elements required in the equivalent circuit. At high negative applied potentials (near V_{OC}), TiO_2 is conductive ($R_t \approx 0$) and the majority of electrons are transferred to the electrolyte from the TiO_2 surface. In this case, the equivalent circuit is reduced to that shown in Figure 12B, and the corresponding Nyquist plot is as shown in Figure 13. The x-axis intersection point of the leftmost side of the Nyquist plot is defined by R_s, followed by three arcs. The first arc on the left (at high frequencies) is due to the counter electrode (parallel R_{CE} and CPE_{CE}), the second (at intermediate frequencies) is from the TiO_2-electrolyte interface (parallel R_{CT} and C_μ), and the third (at low frequencies) from the electrolyte (Z_d). The widths of the arcs are defined by the respective charge-transfer resistances. The arcs are slightly depressed semicircles, indicating that CPEs instead of pure capacitors should be used to describe the interfacial capacitance.

As the applied potential becomes smaller, TiO_2 becomes less conductive, and transport resistance can no longer be neglected. At interemediate potentials, the impedance of the TiO_2 film corresponds to the impedance of the transmission line element in Figure 12A. The whole equivalent circuit of Figure 12A must be used for fitting the EIS response. The intermediate frequency arc starts to dominate the Nyquist plot with increasing contribution from the FTO-electrolyte interface. At low enough applied potentials, TiO_2 becomes insulating, and electrons are transferred to the electrolyte via exposed areas of the FTO

substrate. The Nyquist plot shows a single semiarc displaced from the origin by R_s and perhaps slightly distorted from the edges by the impedances of the counter electrode and electrolyte.

This work focused on studying the DSC EIS response at intermediate to high applied potentials where equivalent circuits of Figure 12 are applicable. The EIS response was recorded in the 0.2–100 000 Hz frequency range. Software packages used for equivalent circuit fittings were LEVMW 8.08[156] and Zview3.3 (Scribner Associates).

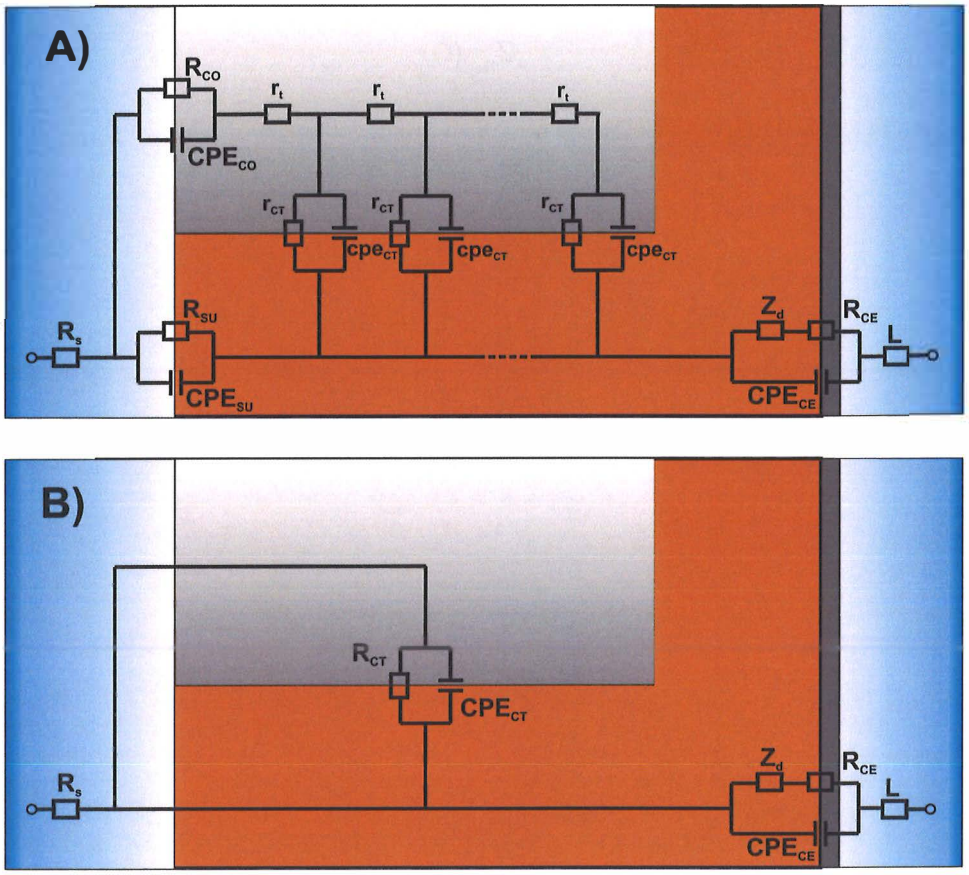

Figure 12 Equivalent circuit for DSC.

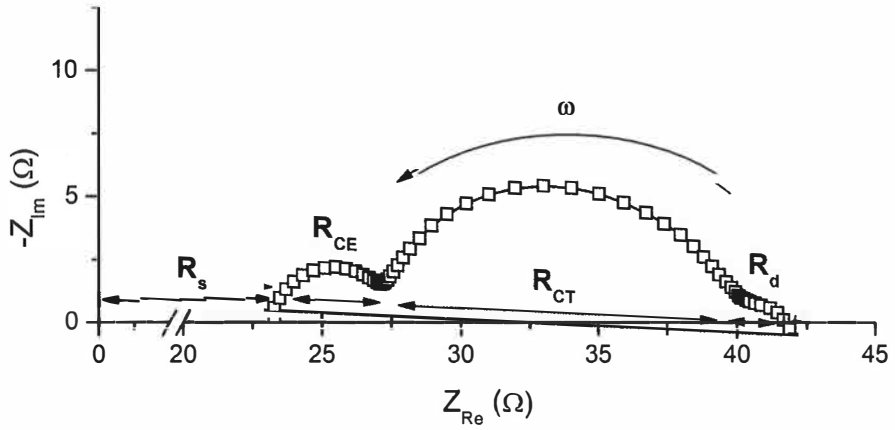

Figure 13 Nyquist plot of a DSC biased near open circuit voltage.

3 RESULTS AND DISCUSSION

3.1 Early electron transfer events in sensitized TiO_2 films in the presence of iodide/triiodide electrolyte

To be able to connect the barrier-induced changes in electron injection to current output in DSCs, it was important to understand the effect of the DSC electrolyte on injection efficiency—especially when it turned out that contradicting interpretations on this effect have been reported in the literature.[68, 71, 73] In Paper I, electron transfer from N3 and N719 dyes to TiO_2 CB was studied in films covered with solvent MPN or with the iodide/triiodide electrolyte. Injection dynamics after excitation at the lower MLCT absorption band was followed by monitoring the transient absorption signals of the oxidized dye in the near-infrared and the injected electrons in the mid-infrared spectral regions. Recording the transient emission from similar sensitized films allowed extending the studies to the nanosecond time domain. Solvent covered films were found to exhibit similar dynamics both in the near- and mid-infrared regions. Time resolution of this experiment did not permit resolving the femtosecond components, but the extracted picosecond components of electron injection were in good agreement with values reported in the literature. It was concluded that N3 and N719 dyes exhibit similar injection kinetics and that injection in solvent covered films takes place mainly in the femto- to picosecond timescale.

In electrolyte covered films, the mid-infrared signal of injected electrons revealed a slowing down of electron injection. The shape of the signal was similar to the decay of transient emission, showing that both methods probe the same phenomenon, the electron injection. The estimated half-time of injection was almost two orders of magnitude longer in electrolyte than in solvent covered films. However, the dye excited state lifetime measured from sensitized Al_2O_3 films was still significantly longer, indicating that injection yield should remain near unity also in the presence of electrolyte.

Comparison of the TA signals of the injected electrons and of the oxidized dye in the presence of the electrolyte revealed significant differences. The picosecond rise signal of the oxidized dye normally observed for sensitized films

covered with neat solvent was barely seen in the presence of the electrolyte. Obviously, an additional process was responsible of the disappearance of this signal. The most probable candidate for this is the reduction of the oxidized dye by the electrolyte I^-, the first step of regeneration (step 1 in Figure 5). Calculations of concentrations profiles of electrolyte anions in acetonitrile show that concentration of iodide peaks at 10 Å from the TiO_2 surface.[81] Intermolecular reactions can easily take place in 1–10 ps over this distance,[157] so the timescale of suggested fast regeneration seems reasonable. To the best of the author's knowledge, this is the first time the dye regeneration step of a ruthenium based DSC using an I^-/I_3^- electrolyte has been observed.

The weak rise of the near-infrared signal in the sub-nanosecond timescale can be tentatively assigned to the formation of (N3···I) or (N719···I) species. Complexation of $Ru(dcbpy)_2(CN)_2$ dye with iodide has been found to draw electron density from the metal center to the CN-ligand, causing increased absorption centered at 750 nm.[86] Similar complex formation of N3 and N719 dyes could result in the survival of the LMCT absorption when the positive charge is removed from the oxidized dye upon reduction. Another possibility is the second step of the regeneration process where the (D···I) complex encounters another iodide and a diiodine ion is released to the electrolyte. The diiodine ion has also been reported to absorb in the same region (absorption and centered at 750 nm)[87, 153] and could therefore contribute to the signal. These assignments could be possibly verified by recording the injection kinetics of $Ru(dcbpy)_2(CN)_2$ in the presence of electrolyte.

3.2 Effect of metal oxide barrier layers on interfacial electron transfer and DSC performance

3.2.1 Characterization of barrier layers

3.2.1.1 Morphology of the layers

Characterization of ALD grown layers grown on nanoporous TiO_2 is not an easy task. In Paper III, the presence of aluminum on the surface of the TiO_2 particles after three ALD cycles was confirmed by energy-dispersive X-Ray spectrometry (EDX). Rutherford backscattering spectrometry was employed to ensure that AlO_x had penetrated throughout the nanoparticle film. The TiO_2 particles coated with three AlO_x ALD cycles were imaged with high-resolution transmission electron microscope (HRTEM) (Paper III, Figure 2). The low contrast between the coating and the nanoparticle prevented accurate determination of the thickness of the AlO_x layer. However, the thickness was estimated to be clearly larger than the 0.3 nm one would expect based on the average Δh reported for the TMA-water process. It is also evident from the HRTEM image that the surface of the coated particle is not smooth.

To obtain information about the molecular structure of the interface after the first ALD cycle, DFT calculations simulating the ALD process were performed.[158] Based on TEM imaging and DFT calculations,[159, 160] the anatase (101) surface is the most exposed facet of the TiO_2 nanoparticles in the DSCs, and it was therefore chosen as the model substrate for the ALD process. Hydration of the surface was modelled by inserting OH-groups and H-atoms on the chosen TiO_2 surface. The TMA molecules were then adsorbed one by one on the surface, and their adsorption energies (E_{ads}) were calculated. It was found that for the first two TMA molecules bound to two of the four sites available on the surface unit cell, the adsorption energies were similar. The E_{ads} for the third molecule was clearly smaller and the adsorption of the fourth molecule was barely exothermic. Based on these calculations, it was concluded that the upper limit for the surface coverage is 50–75% after the first ALD cycle. The areal density of aluminium on the flat TiO_2 anatase surface after the first ALD cycle determined with the ToF-ERDA method supported this conclusion. The water pulse was simulated by replacing the remaining methyl groups in the surface bound TMA molecules with hydroxyl groups. Dye binding to the exposed surface turned out to be unlikely. The dye molecules bound to the $Al(OH)_2$ groups of the layer deposited during the first ALD cycle were thus left at an average distance of 2 Å from the TiO_2 surface. However, the holes in the layer were large enough to fit an iodine atom.

Complete simulation of the second ALD cycle would have required a substantial computational effort; hence, only the binding of a single TMA molecule on top of the first layer was examined. It was found that binding to the exposed TiO_2 surface was practically isoenergetic to binding on top of the AlO_x layer deposited in the first cycle. Therefore, both binding configurations are equally probable suggesting that all holes are not necessarily filled during the second cycle. According to the ToF-ERDA measurements, the GPC was roughly constant during the first five cycles. Based on these results and the calculations, the growth mechanism of AlO_x on the anatase TiO_2 (101) surface seems to be either random or island growth-like, inducing atomic-scale roughness of the deposited layers.

In conclusion, the ALD AlO_x layers seem to be uneven in the atomistic scale and contain holes at least after the first and possibly also after the next few cycles. The distance of the dye molecules from the TiO_2 surface increases faster than the average distances of the iodine species of the electrolyte.

The coverage of HfO_x and TaO_x layers on TiO_2 films was characterized with RBS. For the first HfO_x sample set containing films coated with 1–4 ALD cycles, the penetration of the coating into the bottom of the pores was confirmed. However, for the second HfO_x sample set as well as for the TaO_x samples, the coating had penetrated only through the topmost ~500 nm of both the 2 μm and 6 μm thick TiO_2 films. This was most probably caused by a malfunction of the ALD reactor.

3.2.1.2 Effect of barrier layers on TiO_2 energy levels

UPS measurements were used to determine the effect of the barrier layers on TiO_2 energetics. Incomplete penetration of the coatings was not an issue in these measurements, as the penetration depth of the UV beam is ~10 nm at maximum[142]—much less than the penetration of the coating according to the RBS results. Table 2 shows the valence band maxima (VBM) and work function Φ determined from the UPS spectra of the bare and coated TiO_2 films. Figure 14 shows the relevant metal oxide energy levels.

All studied barrier layer materials had a distinct effect on the energetics of the TiO_2 film. Both the VBM and Fermi level (negative of the work function value) shifted downwards in energy scale (the binding energy of electrons increased) in the coated samples. As the thickness of the metal oxide barrier was increased, the VBM values approached the bulk values of the respective metal oxides. The work function for bare TiO_2 was measured to be 0.4–1 eV smaller than reported in the literature (4.1-4.7 eV).[22, 161] Impurities or exposure to the ambient atmosphere during storage are known to influence the work function,[162] which probably explains the scatter of the obtained and the reported values. In fact, as the surface compositions of metal oxides are strongly affected by preparation and environmental conditions, deductions of semiconductor energetics from the absolute value of the work function should be treated with caution.

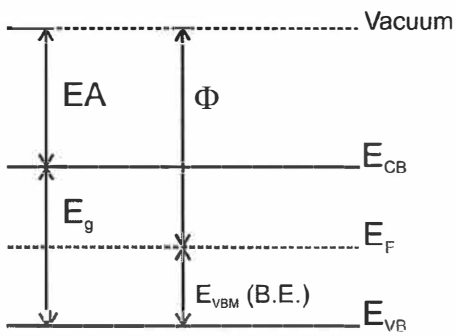

Figure 14 Scheme of semiconductor energy levels. Electron affinity (EA) is equal to the negative of CB energy of the semiconductor and E_g refers to the band gap.

Results from UPS and reflective electron energy loss spectroscopy (REELS) studies[22] also suggest that VBM and EA values approach those of bulk Al_2O_3 upon increasing barrier layer thickness in ALD AlO_x coated TiO_2 films. No estimations about possible E_{CB} shifts could be made from the UPS results. Energetic shifts induced by AlO_x are remarkably larger than that for HfO_x and TaO_x.

Table 2 Valence band maxima and work function determined from UPS spectra of the 2μm thick TiO2 films with and without barrier layers

Sample	Valence band maximum (VBM, $E_{b.e.}$) (eV)[a]	Work function (eV)[b]
TiO_2	3.66 (-7.22)	3.56
AlO_x		
1 cycle	4.14 (-8.34)	4.20
5 cycles	3.93 (-7.44)	3.51
10 cycles	4.55 (-8.47)	3.92
bulk[22]	5.6	
HfO_x		
1 cycle	3.79 (-7.33)	3.54
10 cycles	3.97 (-7.65)	3.68
bulk[163]	4.23	
TaO_x		
1 cycle	3.74 (-7.33)	3.59
10 cycles	3.82 (-7.55)	3.73
28 cycles	3.97 (-7.70)	3.73
bulk[127]	4.03	

[a]Binding energy values of the VBM were determined from the cutting points in the VB region of UPS and are reported relative to the Fermi level (assuming $E_F = 0$). The values in parentheses are given in the vacuum energy scale. [b]Work function values were determined from the values of the cutting points in the secondary electron region of the UPS.

3.2.2 AlOx barrier layers

The studies on the function of barrier layers in DSCs were started with AlO_x because promising results from dip-coated Al_2O_3 barrier layers on DSC performance had been published.[37, 105] An opportunity to optimize the barrier layer thickness and coverage was seen in the use of ALD for growing the barriers. After preliminary tests with 1–4 nm thick layers, the actual studies were started with layers grown with 1–5 ALD cycles.

The effect of AlO_x ALD barrier layers on electron injection was studied in N3-sensitized TiO_2 films covered with MPN by recording the TA signal of the oxidized dye in the near-infrared. The optical densities of the films were carefully matched to allow direct comparison of the signal amplitudes. Figure 1 and Table 1 of Paper II show a comparison between TA signals of N3-sensitized bare TiO_2 and TiO_2 with AlO_x barrier layers grown with 1–5 ALD cycles. It can be seen that all barrier thicknesses lead to the slowing down of singlet injection as the initial amplitude of the signal decreases. Picosecond time constants reflecting triplet injection and their amplitudes remain the same for barriers prepared with 1 or 2 cycles. Although the coupling between the singlet state and the TiO_2 CB states is very strong, it turned out to be sensitive to even small changes of the interface (adiabatic limit). Slowing down of singlet electron injec-

tion was attributed to the weaker coupling between the dye and TiO_2 due to their increased physical separation (~2 Å according to the DFT calculations). In the case of 3 and 5 cycles, the triplet injection also slowed down due to the upward shift of the Fermi level of the TiO_2-AlO_x system.[109] Another paper[22] showed that AlO_x moves TiO_2 E_{CB} upwards in energy (electron affinity decreases), which is a more plausible explanation for the deceleration of triplet injection for barrier layers prepared with more than 3 ALD cycles.

The injection yield relative to the TiO_2 reference sample was determined by calculating the contribution of the oxidized dye to the TA signal. From Figure 2 of Paper II, it can be seen that the injection yield decreased already 15% after the first AlO_x ALD and drastically by 70% after five cycles.

EIS responses of DSCs composed of 2 μm thick TiO_2 films with and without AlO_x barrier layers were recorded near open circuit voltage and near the maximum power point (Paper III). The charge-transfer resistance R_{CT} at the TiO_2-electrolyte interface increased with an increasing number of ALD cycles used to prepare the barriers, while other fitting parameters—including the chemical capacitance of TiO_2, C_μ– remained roughly constant. It was interpreted that the barrier layers affect only the rate of recombination reaction and neither the electron accumulation nor trapping/detrapping dynamics of the TiO_2 film. The effective electron lifetime was calculated from[102, 164]

$$\tau_{eff} = \left(R_{CT} \cdot C_\mu\right)^{1/\beta}, \tag{22}$$

and is related to free electron lifetime τ_f via

$$\tau_{eff} = \frac{C_\mu^{traps}}{C_\mu^{cb}} \tau_f . \tag{23}$$

The lifetime of free electrons is the inverse of the recombination rate. The measured (effective) electron lifetime is mediated by the capture and release of electrons by the trap states and is therefore longer than the free electron lifetime. Since only R_{CT} and not C_μ changed due to the barriers, the changes in effective electron lifetime must be due to changes in recombination rate. Nearly exponential dependence of R_{CT} on the number of AlO_x ALD cycles supported tunnel barrier mechanism of the recombination reaction. The fact that chemical capacitance remained roughly constant indicates that the surface state distribution was not much affected by the barriers.

The current-voltage response of the DSCs without illumination gives information about how easily the TiO_2 electrons are transferred to the electrolyte. The changes in the onset potential of the dark current can be used to estimate shifts of TiO_2 CB energy.[114] However, because the electrolyte cations and additives also cause CB shifts, the observed changes cannot be linked directly to the barrier effects unless the layer is fully continuous. In the case of submonolayer AlO_x barriers, a small (~100 mV) shift of the dark current onset potential was

observed when the layer was grown with more than 3 ALD cycles. This was associated with the combined effect of the electrolyte and the barrier.

Current-voltage response of the DSCs under 1 sun illumination showed decreased current output and conversion efficiency and a small increase in V_{OC} and fill factor with an increasing number of AlO_x ALD cycles. The decrease in J_{SC} followed the decrease in electron injection yield—verifying that injection yields in solvent or in the presence of electrolyte are rather similar. By comparing the injection half-times and effective electron lifetimes, it became clear that injection slowed down more than recombination, leading to the impaired DSC performance observed. One reason for the evident trend in electron transfer rates may be found from the results of the DFT calculations: After the first ALD cycle, the dye could only bind to AlO_x but not to the holes left in the AlO_x layer. However, the calculation indicated that the holes were big enough to fit in iodine atoms. It therefore seems possible that the electron acceptor in the electrolyte, whether I_3^- or I_2, would still be able to reach the TiO_2 surface and capture an electron. This kind of layer structure would produce a larger increase in the average distance from the TiO_2 surface for the dye molecules than for the electrolyte acceptors. This is a plausible explanation for the observed difference in the electron injection and recombination rates. According to the DFT simulation, the TMA precursor binds with equal possibility to the exposed TiO_2 and on top of the AlO_x of the first layer indicating random or island growth-like mechanism. A number of cycles would be needed to obtain full coverage if layer growth proceeded with either of these mechanisms.

The DSCs studied here had rather thin TiO_2 films, so it is expected that their charge collection efficiency is high even without barrier layers; therefore injection yield dominates the current output (Equation 3). Similar J_{SC} behavior has been observed in another system with high η_{CC}, i.e., AlO_x ALD coated ZnO nanotubes.[165] In DSCs with thick (~10 μm) TiO_2 films, the slowing down of recombination can improve η_{CC} significantly, and the current output may be dominated by changes in charge collection rather than injection efficiency. For example, in DSCs with 4 μm TiO_2 films, dip-coated AlO_x barriers had no effect on J_{SC}, while in DSCs with 8 μm TiO_2 films J_{SC} increased when barrier layer was added.[105] A small increase in J_{SC} and η was observed in DSCs with 12 μm TiO_2 films after one AlO_x ALD cycle, but performance deteriorated after two or more cycles.[22, 109] The current output of DSCs depends also on the light-harvesting efficiency (LHE), which can be improved by increasing the dye loading of the film. Al_2O_3 has been shown to adsorb more dye,[105] thereby increasing LHE and contributing to the increase in J_{SC} in cells where the films have been sensitized to saturation.[106, 109]

From this discussion and from the results presented in the literature, it is concluded that for DSCs with TiO_2 films and I^-/I_3^- electrolyte, aluminum oxide is not an optimal barrier layer material. However, in systems where fast recombination is an issue (DSCs with SnO_2 films[122] or ferrocene electrolytes[136]), significant improvement of performance can and has been achieved with AlO_x ALD barrier layers.

3.2.3 HfOx barrier layers

After aluminum oxide turned out to be too insulating even at the smallest thicknesses possible, research gravitated towards hafnium oxide. HfO_2 has a smaller band gap and lower E_{CB} than Al_2O_3, so it was expected that this material would not introduce as strong effects on electron injection as Al_2O_3 (Table 1). Like Al_2O_3, HfO_2 is Lewis-basic, and hence an upward shift of TiO_2 E_{CB} was expected. Since CB of HfO_2 consists of the d-orbitals of Hf^{4+}, it was hoped that the electronic coupling between the dye and TiO_2 would not be as sensitive to the barrier layers as Al_2O_3.

The first preliminary tests were conducted with barrier layers deposited with 1-4 HfO_x ALD cycles using tetrakis(ethylmethylamino)hafnium (TEMAH) and water as precursors. Figure 15 shows the transient absorption signals of N3-sensitized TiO_2 films with HfO_x barrier layers along with the bare TiO_2 and Al_2O_3 references under MPN. Also shown is the TA signal of a N3-sensitized HfO_2 reference film (purple). The film was opaque and scattering and adsorbed dye weakly. The TEM images of the synthesized HfO_2 nanoparticles used to make the film on the FTO substrate revealed aggregation of the particles, which was probably the reason for the poor transparency of the HfO_2 film. The TA trace of the sensitized HfO_2 film in Figure 15 therefore only serves to show the similar shape with the noninjecting Al_2O_3 reference. This implies that light-induced electron injection in sensitized nanocrystalline HfO_2 films is unlikely.

It can be seen from Figure 15 that HfO_x barrier layers decrease the initial (instrument limited) amplitude of the TA signal by 10–20%, while the shape of the picosecond rise is roughly similar for both bare and coated films. The effect of increasing the number of HfO_x ALD cycles on the injection kinetics is clearly smaller than for the same number of AlO_x cycles. Secondly, contrary to the AlO_x coated films, there is no clear correlation between the early signal amplitude and the number of ALD cycles applied on the TiO_2 film. This suggests that the HfO_x barrier layers are more heterogeneous than the AlO_x layers. The DFT simulation of the early steps of the TMA-water process showed the formation of a heterogeneous structure. Using a much bulkier precursor than TMA, it is probable that the TEMAH–water process produces even more heterogeneous layers. Most likely there exists a larger variety of binding sites for the dye molecules in the HfO_x coated TiO_2 films than in the AlO_x coated films. This would at least partly explain the insensitivity of the TA picosecond signals to the number of ALD cycles.

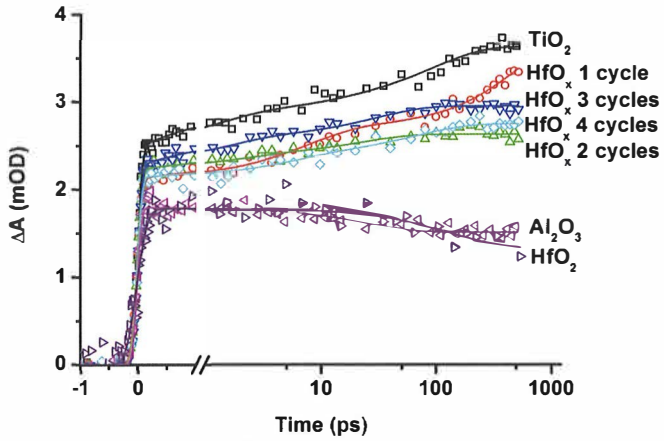

Figure 15 Formation of the oxidized dye probed at 860 nm after excitation at 540 nm of N3-sensitized TiO_2 films with HfO_x barriers layers along with sensitized reference films. Excitation intensity was $2 \cdot 10^{14}$ photons/pulse/cm^2 and IRF 90 fs. Amplitude of the HfO_2 trace was normalized to the amplitude of Al_2O_3 trace for comparison of the shapes of the signals.

EIS measurements were carried out on DSCs with HfO_x barriers: approximately eight cells of a given barrier thickness were measured, and the four most similar selected for analysis. This means that the selected cells had similar charge transfer and series resistances, so differences in their IV-response could be correlated to the modification of the dye-TiO_2-electrolyte –interface.

Figure 16A shows typical Nyquist plots for the measured cells. In cells with HfO_x barriers, the arc corresponding to the counter electrode is buried under the TiO_2-electrolyte arc to the extent that the counter electrode EIS response could not be fitted reliably. Although similar values were obtained for R_{CT} and C_μ whether the counter electrode element was included in the fit or not, the R_{CT} value obtained from the fit cannot be solely assigned to the charge-transfer resistance of the TiO_2-electrolyte interface. Therefore, the changes in effective electron lifetimes shown in Table 3 have to be taken as tentative. However, the increase in dark current onset potentials in Figure 16B correlates to the increase in R_{CT} and τ_{eff}. This indicates that the change in R_{CT} is related to the change in recombination rate.

Current-voltage response of the DSCs with HfO_x barrier layers showed about a 10% decrease in J_{SC} and a small increase in V_{OC} as compared to cells with no barriers (Figure 16B and Table 4). The relative reduction of J_{SC} values for HfO_x barrier layers are clearly smaller than for the AlO_x barrier layers with corresponding number of ALD cycles. A small increase in the onset potential of dark current was observed, which along with the small increase in R_{CT}, indicated that recombination slowed down slightly. This behavior is very different to that observed for AlO_x coatings that hindered the recombination reactions efficiently. The studied HfO_x barriers did not reduce the conversion efficiency of the prepared cells within experimental error.

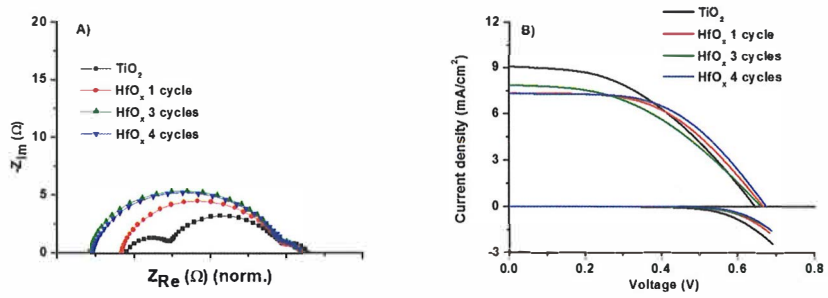

Figure 16 A) Examples of Nyquist plots of DSCs prepared from 2 μm thick TiO_2 films with HfO_x barrier layers and a reference DSC without the barrier measured at 0.65 V bias under illumination. The plots are normalized to the same Z_{Re} at the intersection of the two right-most arcs to allow better comparison of the charge-transfer resistances of the photoactive electrodes. **B)** Current-voltage responses of the same cells under illumination and in the dark. Illumination intensity was 1.4 suns.

Table 3 Parameters obtained from fitting the Nyquist plots of similar DCSs than shown in Figure 16. Only parameters relevant to the photoactive electrode are shown.

Number of ALD cycles	0	1 cycle of HfO_x	3 cycles of HfO_x	4 cycles of HfO_x
R_{CT} (Ω)	9 ± 1	8 ± 2	11± 2	12 ± 2
C_μ (mF)	0.87 ± 0.01	0.7 ± 0.5	0.9 ± 0.2	0.8 ± 0.2
β_μ	0.85 ± 0.03	0.96 ± 0.04	0.88 ± 0.01	0.87 ± 0.02
τ_{eff} (ms)	3.4 ± 1.2	4 ± 3	5 ± 1	5 ± 1

Table 4 Characteristic parameters of DSCs prepared from 2 μm thick TiO_2 films with and without HfOx barrier layers under 1.4 sun illumination.

Number of HfO_x ALD cycles	0	1	3	4
J_{SC} (mA/cm^2)	9.0 ± 0.4	7.3 ± 0.4	7.9 ± 0.3	7.3 ± 0.2
V_{OC} (V)	0.64 ± 0.02	0.67 ± 0.02	0.66 ± 0.02	0.66 ± 0.01
Efficiency (%)	2.6 ± 0.3	2.5 ± 0.1	2.3 ± 0.2	2.6 ± 0.4
Fill Factor	0.44 ± 0.06	0.51 ± 0.04	0.43 ± 0.04	0.54 ± 0.08

The detrimental effect of the HfO_x barrier layers on electron injection and current output of the DSCs seems to be independent of the number of ALD cycles used for the deposition—at least in the case of the studied submonolayers. Therefore, a moderate increase in the number of cycles would not necessarily lead to any additional decrease in injection yield. To have a clear impact on re-

combination with HfO_x barrier material, one would need to increase the number of barrier layers from what was used in the present study.

Reduction of the recombination reaction rate due to barrier layers is expected to have a stronger effect on the charge collection efficiency in thick rather than in thin TiO_2 films. Therefore, both thin (2 μm) and thick (6 μm) TiO_2 films were coated with HfO_x barrier layers in the next phase of the work. The EIS responses were recorded for a wider range of bias potentials (0.3-0.6 V) to determine R_{CT} more reliably for the DSCs with HfO_x barriers. Two limiting barrier thicknesses were prepared: one with only one HfO_x ALD cycle and the other with 12 ALD cycles. It was found out from RBS measurements of these samples that the coatings had only penetrated ~500 nm from the topmost surface of the TiO_2 film. The TA signals of the sensitized films with barriers prepared with 12 HfO_x ALD cycles had about 5% smaller initial rise amplitude than the reference TiO_2 films. In IV and EIS experiments, practically no differences were observed between DSCs with and without barrier layers.

The question whether HfO_x barrier layers can be used to improve DSC performance remains open with the results at hand. In the literature,[166] HfO_x barrier layers prepared by the $HfCl_4$–water process by applying 5 ALD cycles of on 6 μm thick TiO_2 films improved DSC conversion efficiency by 70%. However, the authors gave results for their best cells, so it is difficult to judge whether the results were reproducible from cell to cell. If the results are to be trusted, then the reason for their success could be the smaller size of the HfO_x precursor that could have created smoother layers than the bulkier TEMAH precursor used in the present study.

3.2.4 TaOx barrier layers

Considering the bulk metal oxide properties listed in Table 1, Ta_2O_5 is less insulating than HfO_2 since its band gap is only slightly larger than that of TiO_2. However, the CB energy of Ta_2O_5 is still at least 0.6 eV higher than E_{CB} of TiO_2. Like HfO_2, the CB of Ta_2O_5 is constructed of d-orbitals, but while HfO_2 is a Lewis base, Ta_2O_5 is acidic. If the metal oxide barrier layers affected the TiO_2 CB energy like Lewis acid species of the electrolyte, a downward shift of E_{CB} and an improvement of electron injection yield could be expected with TaO_x barrier layers.

Poor penetration of the coating to the nanopores of the TiO_2 film was an issue also for the TaO_x barriers. The studied coatings were deposited with 1 or 28 cycles with the $Ta(OEt)_5$-water process and similar penetration depth of 500 nm as for the HfO_x coated samples was found in the RBS-measurements. However, unlike for HfO_x, significant effects on electron injection and current output of DSCs were observed with TaO_x barriers. Figure 17 shows the TA signals of N3-sensitized TiO_2 films with and without partial TaOx barrier layers (28 ALD cycles) in MPN. Shown also in Figure 17 is the TA signal of a sensitized Ta_2O_5 reference film. No electron injection seems to take place into nanocrystalline

Ta_2O_5. UPS results (Section 3.2.1.2) show that the 28-cycle sample has similar VBM as bulk Ta_2O_5, but the CB energy must be lower than that of bulk oxide considering the increased injection in the coated sample.

It can be seen from Figure 17 that in the film with a TaO_x barrier, the initial amplitude is 10% higher than in the bare TiO_2 film. Table 5 shows the time constants obtained by fitting a sum of three exponentials to the data. Time constants for the formation of oxidized dye in the bare TiO_2 film are similar to those reported in Papers I and II. It can be concluded that the barrier layers do not affect kinetics of triplet injection. From Figure 17, it is clear that TaO_x improves the efficiency of singlet injection. This finding is remarkable in the sense that until now, no barrier layer material has been shown to actually improve injection into TiO_2.

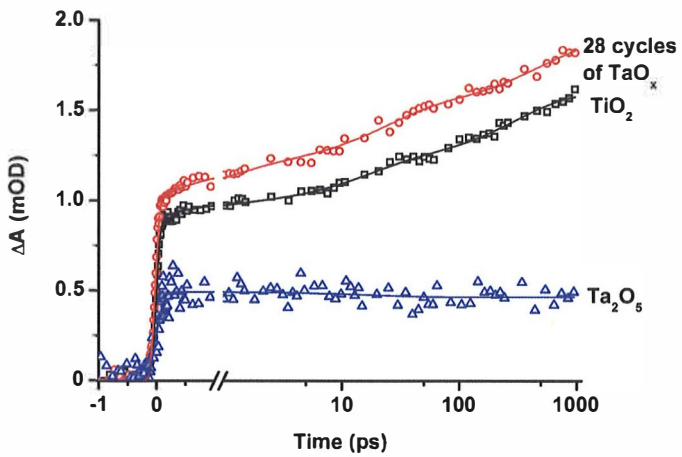

Figure 17 Formation of oxidized dye probed at 860 nm after excitation at 540 nm of N3-sensitized TiO_2 films with and without TaO_x barrier layers. Excitation intensity was $3 \cdot 10^{14}$ photons/pulse/cm^2 and IRF 86 fs.

Table 5 Time constants (τ) and relative amplitudes (in percentages of total amplitude) obtained from fitting transient absorption signals in **Figure 17**.

	τ_1 (A_1)	τ_2 (A_2)	τ_3 (A_3)	τ_4 (A_4)
TiO_2	< 100fs (55%)	0.6 ps (5%)	15 ps (15%)	300 ps (25%)
28 cycles of TaO_x	< 100fs (50%)	1.1 ps (10%)	22 ps (20%)	500 ps (20%)

EIS responses of DSCs containing 2 μm thick TiO_2 films with TaO_x barrier layers were measured at four different bias voltages (0.3-0.6 V) in the frequency range of 1–100 000 Hz. The Nyquist plot was fitted with ZView3.3 software to apply the transmission line element to the impedance of the photoactive electrode at intermediate voltages. Figure 18 shows the voltage dependence of the EIS parameters related to the photoactive electrode obtained from the fits. It can be seen that the barrier layer does not affect charge-transfer resistances R_{CT} nor

R_T but increases the chemical capacitance C_μ of the film. This leads to an increase in effective electron lifetime τ_{eff} (Figure 18D). The values in Table 6 show that there is actually a small decrease in R_{CT}, while C_μ and τ_{eff} are doubled in cells with barriers grown with 28 cycles compared to cells with no barriers. If the TiO_2 CB energy was shifted downwards by the TaO_x barrier layer, it would have been revealed in the voltage dependence of transport resistance since in a cell with a downward shifted E_{CB}, a lower voltage would have been required to reach the same R_T value as in the reference cell.[37] On the other hand, as the TiO_2 films are only partially coated, the induced shift would not be as noticeable as for a fully penetrated barrier layer.

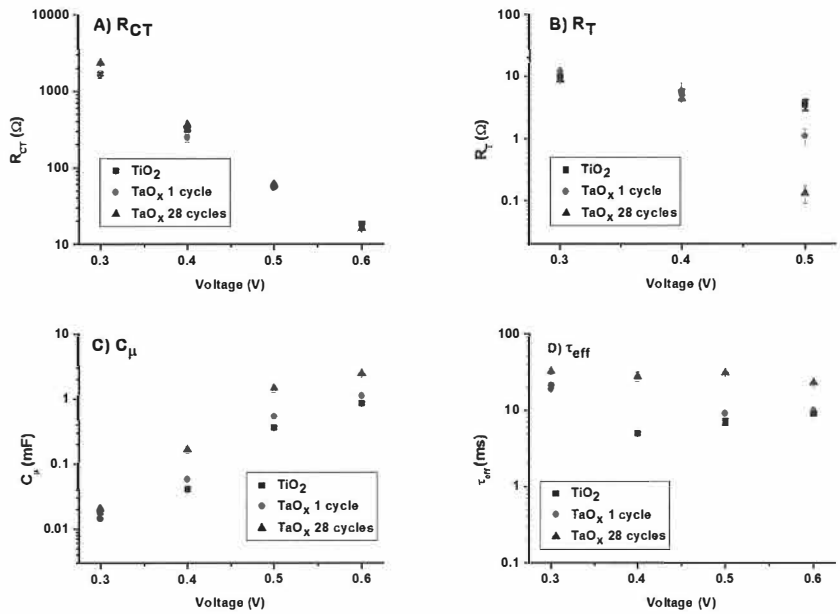

Figure 18 EIS parameters of photoactive electrode of DSCs with 2 μm thick TiO_2 films with and without partial TaO_x barrier layers as function of bias potential.

Table 6 EIS parameters of photoactive electrode of DSCs prepared from 2 μm thick TiO_2 films with and without TaO_x barrier layers at 0.6 V bias voltage.

Number of ALD cycles	TiO_2	1 cycle of TaO_x	28 cycles of TaO_x
R_{CT} (Ω)	18.6 ± 0.14	17.7 ± 0.3	16.3± 0.1
C_μ (mF)	0.87 ± 0.03	1.14 ± 0.02	2.48 ± 0.05
β_μ	0.88 ± 0.01	0.85 ± 0.01	0.85 ± 0.07
τ_{eff} (ms)	9.0 ± 0.3	9.9 ± 0.2	22.7 ± 0.9

Current-voltage responses of DSCs with TaO_x barrier layers (Table 7) grown with 28 ALD cycles show higher current output and conversion efficiency than DCSs without barriers. V_{OC} and fill factor remained roughly the same. The increase in J_{SC} is of the same magnitude (15%) as the increase in the singlet injection amplitude (10%). The increased injection is also probably the underlying reason for the increased C_μ. Recombination is not much affected by the TaO_x barriers; therefore V_{OC} does not increase. The increase in injection could be caused by a downward shift of the TiO_2 CB or by improved coupling between the dye and TiO_2 induced by the dye binding to TaO_x. However, the current data cannot provide conclusive information on this mechanism, so investigating this subject further is left for future studies.

Number of TaO_x ALD cycles	**0**	**1**	**28**
J_{SC} (mA/cm^2)	6.3 ± 0.3	6.1 ± 0.2	7.3 ± 0.2
V_{OC} (V)	0.64 ± 0.01	0.63 ± 0.01	0.64 ± 0.01
Efficiency (%)	2.5 ± 0.1	2.4 ± 0.1	3.0 ± 0.2
Fill Factor	0.61 ± 0.04	0.63 ± 0.04	0.63 ± 0.05

Table 7 Characteristic parameters of DSCs prepared from 2 μm thick TiO_2 films with and without TaO_x barrier layers under 1 sun illumination.

It is surprising that the TaO_x barriers have a positive effect on the electron injection and current output of the DSCs even though they are covering only a quarter of the TiO_2 film thickness. Unfortunately, in the DSCs made from 6 μm thick films with barriers, no effect could be seen, but then again for these films, less than 10% of the surface area is coated. Nevertheless, TaO_x appears to be a promising material for barrier layers: since the electron injection is enhanced even when the layers are grown with 28 cycles, it would be possible to use thick and continuous TaO_x barriers without damage to the injection. These layers would efficiently protect the TiO_2 surface from the electron acceptors of the electrolyte. The only disadvantage would arise from the possible downward shift of TiO_2 CB that would decrease the obtainable V_{OC} from the cells. To answer these questions, the experiments need to be repeated with barrier layers covering the entire depth of the TiO_2 film.

3.2.5 Summary on barrier layer studies

The studied barrier layers affected the singlet injection even after the first ALD metal oxide cycle, independent of the oxide studied. Current outputs of the DSCs with barrier layers correlated with the changes in the TA response ampli-

tudes corresponding to singlet state injection measured for the photoactive electrodes. AlO_x barrier layers had the strongest impact on forward electron injection and hence the ET coupling between the dye and the electron acceptor. Slowing down of recombination was evident for the AlO_x barrier layers and was probably caused by blocking the access of the electrolyte electron acceptors to the TiO_2 surface. For HfO_x coatings, the reduction of electron injection efficiency was roughly the same for one as well as for 4-cycle ALD coatings. EIS measurements suggested that for this coating material, thicker barrier layers are needed to obtain reductions in recombination reactions of the cell. TA results indicate this can be done without much sacrificing on injection efficiency. Surprisingly, for relatively thick TaO_x coatings (28 cycles), a 15% improvement in electron injection efficiency was observed. For these samples, the penetration of the coating was not complete, and hence the true effect of the barrier on the recombination reactions could not be quantitatively established. Yet, even with this incomplete penetration of the oxide, improvement of the short circuit current and cell efficiency was observed.

The changes in electron transfer rates can be partially ascribed to the shifting of TiO_2 energy levels due to barrier layers. The barriers had a distinct effect on the valence band maxima of the films, so it is likely that conduction band energy was also affected. The magnitude and direction of the CB level shift could not be quantitatively resolved from our data.

Hafnium and tantalum oxide studies should be repeated in DSCs with thick (~10 μm) TiO_2 films in order to specify whether the effect of the barrier layer on injection or recombination dominates the current output and performance of the cell. For HfO_x barriers, employing smaller precursor molecules could be beneficial as there is a possibility to produce high coverage of the TiO_2 film with a smaller number of cycles. This could result in more effective retardation of recombination with less damage to the injection. The interesting question for TaO_x is whether a full coverage barrier layer leads to a decrease in V_{OC} and if this effect can be outweighed by increased current output.

Another interesting barrier layer material would be niobium oxide, as it is also a Lewis acid like Ta_2O_5 and therefore has a potential to lower TiO_2 CB (Table 1). In addition, Nb_2O_5 has a high density of conduction band states. These features are promising considering electron injection in sensitized films with these barriers. Nb_2O_5 films have been reported to perform well as photoactive electrodes of DSCs.[79]

4 CONCLUSIONS

This thesis focused on the electron transfer reactions taking place at the photoactive electrode of dye-sensitized solar cells: electron injection, early steps of dye regeneration, and recombination of the injected electron with electrolyte species. Correlations between electron injection rates and the performance of complete DSCs were also investigated.

It was demonstrated that electron injection from two ruthenium based dyes to nanocrystalline TiO_2 slowed down significantly in the presence of iodide/triiodide electrolyte compared to the neat electrolyte solvent. The rate of injection still remained rapid compared to the decay of the dye excited state. Comparison of the transient absorption signals of the oxidized dye and injected electron signals in the presence of the electrolyte revealed the reduction of the oxidized dye in the picosecond time domain. To the best of the author's knowledge, this is the first observation of the initial steps of dye regeneration in this time scale, more than 20 years after the invention of the cell. This observation also paves the way for the understanding of the mechanisms of the entire redox cycle of the cell.

The major part of the work dealt with the effect of metal oxide barrier layers on interfacial electron transfer—both electron injection and recombination. Atomic layer deposition was used for preparation of protective barrier layers on the nanocrystalline TiO_2 films that form the photoactive electrode of the dye-sensitized solar cells. It was observed that layers of just a few ALD cycles thick can have drastic effects on electron transfer and the performance of the cell. Aluminum oxide barrier layers retarded injection more than recombination even after one ALD cycle and therefore led to impaired DSC performance. Experiments of hafnium oxide barriers prepared with up to 4 ALD cycles slowed down injection but did not deter the DSC performance to the same extent as aluminum oxide barriers. Coverage of hafnium oxide on the TiO_2 film was not perfect, which meant that recombination reactions were not slowed down at full potential. Surprisingly, relatively thick (~1 nm) tantalum oxide barrier layers improved electron injection efficiency and current output of the DSCs. No other barrier layer material has so far been reported to enhance injection. The

finding is significant also in the sense that the observed improvements were induced by a layer covering only about one quarter of the surface of the TiO_2 film.

BIBLIOGRAPHY

1. www.iea.org/publications/, International Energy Agency, retrieved 27.02.2013.

2. *International Energy Outlook 2011,* , U.S. Energy Information Administration, Washington, D.C., US, 2011.

3. www.bp.com/statisticalreview, retrieved 27.02.2013.

4. Chapin, D.M., Fuller, C.S., Pearson, G.L., *J. Appl. Phys.* **1954**, *25,* 676.

5. Hagfeldt, A., Boschloo, G., Sun, L., Kloo, L., Pettersson, H., *Chem Rev.* **2010**, *110,* 6595-6663.

6. O'Regan, B. and Grätzel, M., *Nature.* **1991**, *353,* 737-740.

7. Yella, A., Lee, H., Tsao, H.N., Yi, C., Chandiran, A.K., Nazeeruddin, M.K., Diau, E.W., Yeh, C., Zakeeruddin, S.M., Grätzel, M., *Science.* **2011**, *334,* 629-634.

8. Chung, I., Lee, B., He, J., Chang Robert, P.H., Kanatzidis, M.G., *Nature.* **2012**, *485,* 486-489.

9. Michael Grätzel, Hybrid and Organic Photovoltaics Conference HOPV2013, Seville, Spain, May 7th, 2013.

10. Burschka, J., Pellet, N., Moon, S., Humphry-Baker, R., Gao, P., Nazeeruddin, M.K., Graetzel, M., *Nature.* **2013**, *499,* 316-319.

11. Kalyanasundaram,K., *Dye-sensitized solar cells.* Anonymous EPFL Press, Lausanne, Switzerland, 2010, pp.

12. Nazeeruddin, M.K., Kay, A., Rodicio, I., Humphry-Baker, R., Mueller, E., Liska, P., Vlachopoulos, N., Grätzel, M., *J. Am. Chem. Soc.* **1993**, *115,* 6382-6390.

13. Nazeeruddin, M.K., Zakeeruddin, S.M., Humphry-Baker, R., Jirousek, M., Liska, P., Vlachopoulos, N., Shklover, V., Fischer, C., Grätzel, M., *Inorg. Chem.* **1999**, *38,* 6298-6305.

14. Montanari, I., Nelson, J., Durrant, J.R., *J. Phys. Chem. B.* **2002**, *106,* 12203-12210.

15. Reference Solar Spectral Irradiance: Air Mass 1.5, http://rredc.nrel.gov/solar/spectra/am1.5/, American Society for Testing and Materials, retrieved July 1st, 2013.

16. Kumar, A., Santangelo, P.G., Lewis, N.S., *J. Phys. Chem.* **1992**, *96,* 834-842.

17. O'Regan, B., Moser, J., Anderson, M., Grätzel, M., *J. Phys. Chem.* **1990**, *94,* 8720-8726.

18. Kopidakis, N., Schiff, E.A., Park, N.-., van de Lagemaat, J., Frank, A.J., *J. Phys. Chem.* **2000**, *104,* 3930-3936.

19. Madhusudan Reddy, K., Gopal Reddy, C.V., Manorama, S.V., *J. Solid State Chem.* **2001**, *158,* 180-186.

20. Liu, Y., Hagfeldt, A., Xiao, X., Lindquist, S., *Sol. Energ. Mat. Sol. Cells.* **1998**, *55,* 267-281.

21. Schwanitz, K., Weiler, U., Hunger, R., Mayer, T., Jaegermann, W., *J. Phys. Chem. C.* **2007**, *111,* 849-854.

22. Tien, T., Pan, F., Wang, L., Lee, C., Tung, Y., Tsai, S., Lin, C., Tsai, F., Chen, S., *Nanotechnology.* **2009**, *20,* 305201/1-305201/8.

23. Moser, J., Punchihewa, S., Infelta, P.P., Graetzel, M., *Langmuir.* **1991**, *7,* 3012-3018.

24. Sanjines, R., Tang, H., Berger, H., Gozzo, F., Margaritondo, G., Levy, F., *J. Appl. Phys.* **1994**, *75,* 2945-2951.

25. Salvador, P., Hidalgo, M.G., Zaban, A., Bisquert, J., *J. Phys. Chem. B.* **2005**, *109,* 15915-15926.

26. Cao, F., Oskam, G., Meyer, G.J., Searson, P.C., *J. Phys. Chem.* **1996**, *100,* 17021-17027.

27. de Jongh, P.E. and Vanmaekelbergh, D., *Phys. Rev. Lett.* **1996**, *77,* 3427-3430.

28. Nelson, J. and Chandler, R.E., *Coord. Chem. Rev.* **2004**, *248,* 1181-1194.

29. Bisquert, J. and Vikhrenko, V.S., *J. Phys. Chem. B.* **2004**, *108,* 2313-2322.

30. Gonzalez-Vazquez, J., Oskam, G., Anta, J.A., *J. Phys. Chem. C.* **2012**, *116,* 22687-22697.

31. Rothenberger, G., Fitzmaurice, D., Grätzel, M., *J. Phys. Chem.* **1992**, *96,* 5983-5986.

32. Redmond, G. and Fitzmaurice, D., *J. Phys. Chem.* **1993**, *97,* 1426-1430.

33. Zhang, C., Huang, Y., Huo, Z., Chen, S., Dai, S., *J. Phys. Chem. C.* **2009**, *113,* 21779-21783.

34. Yu, Z., Gorlov, M., Boschloo, G., Kloo, L., *J. Phys. Chem. C.* **2010**, *114,* 22330-22337.

35. Schlichthorl, G., Huang, S.Y., Sprague, J., Frank, A.J., *J. Phys. Chem. B.* **1997**, *101,* 8141-8155.

36. Boschloo, G., Haggman, L., Hagfeldt, A., *J. Phys. Chem. B.* **2006**, *110,* 13144-13150.

37. Fabregat-Santiago, F., Bisquert, J., Garcia-Belmonte, G., Boschloo, G., Hagfeldt, A., *Sol. Energ. Mat. Sol. Cells.* **2005**, *87,* 117-131.

38. Wang, Q., Zhang, Z., Zakeeruddin, S.M., Grätzel, M., *J. Phys. Chem. C.* **2008**, *112,* 7084-7092.

39. Koops, S.E., O'Regan, B.C., Barnes, P.R.F., Durrant, J.R., *J. Am. Chem. Soc.* **2009**, *131,* 4808-4818.

40. Katz, M.J., Vermeer, M.J.D., Farha, O.K., Pellin, M.J., Hupp, J.T., *Langmuir.* **2013**, *29,* 806-814.

41. Asbury, J.B., Hao, E., Wang, Y., Ghosh, H.N., Lian, T., *J. Phys. Chem. B.* **2001**, *105,* 4545-4557.

42. Asbury, J.B., Anderson, N.A., Hao, E., Ai, X., Lian, T., *J. Phys. Chem. B.* **2003**, *107,* 7376-7386.

43. Clifford, J.N., Palomares, E., Nazeeruddin, M.K., Grätzel, M., Nelson, J., Li, X., Long, N.J., Durrant, J.R., *J. Am. Chem. Soc.* **2004**, *126,* 5225-5233.

44. Guo, J., She, C., Lian, T., *J. Phys. Chem. C.* **2007**, *111,* 8979-8987.

45. Marcus, R.A., *J. Chem. Phys.* **1956**, *24,* 966-978.

46. Miller,R.J.D., McLendon,G.L., Nozik,A.J., Schmikler,W. and Willig,F., *Surface Electron Transfer Processes.* Edition, VCH Publishers, Inc., USA, 1995.

47. Bolton,J.R. and Archer,M.D., *Electron Transfer in Inorganic, Organic, and Biological Systems,* 1st. Edition, American Chemical Society, Washington DC, US, 1991, ss. 7-22.

48. Schiffmann, F., VandeVondele, J., Hutter, J., Wirz, R., Urakawa, A., Baiker, A., *J. Phys. Chem. C.* **2010**, *114,* 8398-8404.

49. De Angelis, F., Fantacci, S., Mosconi, E., Nazeeruddin, M.K., Grätzel, M., *J. Phys. Chem. C.* **2011**, *115,* 8825-8831.

50. Persson, P. and Lundqvist, M.J., *J. Phys. Chem. B.* **2005**, *109,* 11918-11924.

51. Nazeeruddin, M.K., De Angelis, F., Fantacci, S., Selloni, A., Viscardi, G., Liska, P., Ito, S., Takeru, B., Graetzel, M., *J. Am. Chem. Soc.* **2005**, *127,* 16835-16847.

52. Nazeeruddin, M.K., Humphry-Baker, R., Liska, P., Grätzel, M., *J. Phys. Chem. B.* **2003**, *107,* 8981-8987.

53. Ardo, S., Sun, Y., Staniszewski, A., Castellano, F.N., Meyer, G.J., *J. Am. Chem. Soc.* **2010**, *132,* 6696-6709.

54. De Angelis, F., Fantacci, S., Selloni, A., *Nanotechnology.* **2008**, *19,* 424002/1-424002/7.

55. Tachibana, Y., Moser, J.E., Grätzel, M., Klug, D.R., Durrant, J.R., *J. Phys. Chem.* **1996**, *100,* 20056-20062.

56. Benkö, G., Kallioinen, J., Korppi-Tommola, J., Yartsev, A.P., Sundström, V., *J. Am. Chem. Soc.* **2002**, *124,* 489-493.

57. Benkö, G., Kallioinen, J., Myllyperkiö, P., Trif, F., Korppi-Tommola, J., Yartsev, A.P., Sundström, V., **2004**, *108,* 2862-2867.

58. Kallioinen, J., Benkö, G., Sundström, V., Korppi-Tommola, J., Yartsev, A.P., *J. Phys. Chem. B.* **2002**, *106,* 4396-4404.

59. Benkö, G., Myllyperkio, P., Pan, J., Yartsev, A.P., Sundström, V., *J. Am. Chem. Soc.* **2003**, *125,* 1118-1119.

60. Pellnor, M., Myllyperkiö, P., Korppi-Tommola, J., Yartsev, A., Sundström, V., *Chem. Phys. Lett.* **2008**, *462,* 205-208.

61. Myllyperkiö, P., Benkö, G., Korppi-Tommola, J., Yartsev, A.P., Sundström, V., *Phys. Chem. Chem. Phys.* **2008**, *10,* 996-1002.

62. Tachibana, Y., Haque, S.A., Mercer, I.P., Durrant, J.R., Klug, D.R., *J. Phys. Chem. B.* **2000**, *104,* 1198-1205.

63. Tachibana, Y., Haque, S.A., Mercer, I.P., Moser, J.E., Klug, D.R., Durrant, J.R., *J. Phys. Chem. B.* **2001**, *105,* 7424-7431.

64. Kallioinen, J., Lehtovuori, V., Myllyperkio, P., Korppi-Tommola, J., *Chem. Phys. Lett.* **2001**, *340,* 217-221.

65. Kallioinen, J., Benkö, G., Myllyperkiö, P., Khriachtchev, L., Skårman, B., Wallenberg, R., Tuomikoski, M., Korppi-Tommola, J., Sundström, V., Yartsev, A.P., *J. Phys. Chem. B.* **2004**, *108,* 6365-6373.

66. Katoh, R., Fuke, N., Furube, A., Koide, N., *Chem. Phys. Lett.* **2010**, *489,* 202-206.

67. Kuciauskas, D., Monat, J.E., Villahermosa, R., Gray, H.B., Lewis, N.S., McCusker, J.K., *J. Phys. Chem. B.* **2002**, *106,* 9347-9358.

68. Haque, S.A., Palomares, E., Cho, B.M., Green, A.N.M., Hirata, N., Klug, D.R., Durrant, J.R., *J. Am. Chem. Soc.* **2005**, *127,* 3456-3462.

69. Wenger, B., Graetzel, M., Moser, J., *J. Am. Chem. Soc.* **2005**, *127,* 12150-12151.

70. Katoh, R., Furube, A., Yoshihara, T., Hara, K., Fujihashi, G., Takano, S., Murata, S., Arakawa, H., Tachiya, M., *J. Phys. Chem. B.* **2004**, *108,* 4818-4822.

71. Teuscher, J., Décoppet, J., Punzi, A., Zakeeruddin, S.M., Moser, J., Grätzel, M., *J. Phys. Chem. Lett.* **2012**, *3,* 3786-3790.

72. Tachibana, Y., Nazeeruddin, M.K., Grätzel, M., Klug, D.R., Durrant, J.R., *Chem. Phys.* **2002**, *285,* 127-132.

73. Juozapavicius, M., Kaucikas, M., van Thor, J.J., O'Regan, B.C., *J. Phys. Chem. C.* **2013**, *117,* 116-123.

74. Bräm, O., Cannizzo, A., Chergui, M., *Phys. Chem. Chem. Phys.* **2012**, *14,* 7934-7937.

75. Koops, S.E. and Durrant, J.R., *Inorg. Chim. Acta.* **2008**, *361,* 663-670.

76. Barnes, P.R.F., Anderson, A.Y., Koops, S.E., Durrant, J.R., O'Regan, B.C., *J. Phys. Chem. C.* **2009**, *113,* 1126-1136.

77. Nemec, H., Rochford, J., Taratula, O., Galoppini, E., Kuzel, P., Polivka, T., Yartsev, A., Sundstrom, V., *Phys. Rev. Lett.* **2010**, *104,* 197401/1-197401/4.

78. Pijpers, J.J.H., Ulbricht, R., Derossi, S., Reek, J.N.H., Bonn, M., *J. Phys. Chem. C.* **2011**, *115,* 2578-2584.

79. Sayama, K., Sugihara, H., Arakawa, H., *Chem. Mat.* **1998**, *10,* 3825-3832.

80. Kelly, C.A., Farzad, F., Thompson, D.W., Stipkala, J.M., Meyer, G.J., *Langmuir.* **1999**, *15,* 7047-7054.

81. Schiffmann, F., Vandevondele, J., Hutter, J., Urakawa, A., Wirz, R., Baiker, A., *Proc. Natl. Acad. Sci. U. S. A.* **2010**, *107,* 4830-4833, S4830/1-S4830/2.

82. Anderson, A.Y., Barnes, P.R.F., Durrant, J.R., O'Regan, B.C., *J. Phys. Chem. C.* **2011**, *115,* 2439-2447.

83. Boschloo, G. and Hagfeldt, A., *Acc. Chem. Res.* **2009**, *42,* 1819-1826.

84. Gardner, J.M., Abrahamsson, M., Farnum, B.H., Meyer, G.J., *J. Am. Chem. Soc.* **2009**, *131,* 16206-16214.

85. Rowley, J.G., Ardo, S., Sun, Y., Castellano, F.N., Meyer, G.J., *J. Phys. Chem. C.* **2011**, *115,* 20316-20325.

86. Clifford, J.N., Palomares, E., Nazeeruddin, M.K., Grätzel, M., Durrant, J.R., *J. Phys. Chem. C.* **2007**, *111,* 6561-6567.

87. Tuikka, M., Hirva, P., Rissanen, K., Korppi-Tommola, J., Haukka, M., *Chem. Commun.* **2011**, *47,* 4499-4501.

88. Gerischer, H., *Z. Phys. Chem.* **1960**, *26,* 223-247.

89. Gerischer, H., *Z. Phys. Chem.* **1960**, *26,* 325-338.

90. Memming, R., *Prog. Surf. Sci.* **1984**, *17,* 7-73.

91. Bisquert, J., Zaban, A., Greenshtein, M.M.,I., *J. Am. Chem. Soc.* **2004**, *126,* 13550-13559.

92. Nakade, S., Kanzaki, T., Kubo, W., Kitamura, T., Wada, Y., Yanagida, S., *J. Phys. Chem. B.* **2005**, *109,* 3480-3487.

93. Boschloo, G., Gibson, E.A., Hagfeldt, A., *J. Phys. Chem. Lett.* **2011**, *2,* 3016-3020.

94. Mori, S.N., Kubo, W., Kanzaki, T., Masaki, N., Wada, Y., Yanagida, S., *J. Phys. Chem. C.* **2007**, *111,* 3522-3527.

95. Anderson, A.Y., Barnes, P.R.F., Durrant, J.R., O'Regan, B.C., *J. Phys. Chem. C.* **2010**, *114,* 1953-1958.

96. Haque, S.A., Tachibana, Y., Klug, D.R., Durrant, J.R., *J. Phys. Chem. B.* **1998**, *102,* 1745-1749.

97. Pelet, S., Moser, J., Graetzel, M., *J. Phys. Chem. B.* **2000**, *104,* 1791-1795.

98. Haque, S.A., Tachibana, Y., Willis, R.L., Moser, J.E., Grätzel, M., Klug, D.R., Durrant, J.R., *J. Phys. Chem. B.* **2000**, *104,* 538-547.

99. Kuciauskas, D., Freund, M.S., Gray, H.B., Winkler, J.R., Lewis, N.S., *J. Phys. Chem. B.* **2001**, *105,* 392-403.

100. Green, A.N.M., Palomares, E., Haque, S.A., Kroon, J.M., Durrant, J.R., *J. Phys. Chem. B.* **2005**, *109,* 12525-12533.

101. Jennings, J.R. and Wang, Q., *J. Phys. Chem. C.* **2010**, *114,* 1715-1724.

102. Bisquert, J., Fabregat-Santiago, F., Mora-Seró, I., Garcia-Belmonte, G., Giménez, S., *J. Phys. Chem. C.* **2009**, *113,* 17278-17290.

103. Wang, Q., Ito, S., Grätzel, M., Fabregat-Santiago, F., Mora-Seró, I., Bisquert, J., Bessho, T., Imai, H., *J. Phys. Chem. B.* **2006**, *110,* 25210-25221.

104. Richards, C.E., Anderson, A.Y., Martiniani, S., Law, C., O'Regan, B.C., *J. Phys. Chem. Lett.* **2012**, *3,* 1980-1984.

105. Palomares, E., Clifford, J.N., Haque, S.A., Lutz, T., Durrant, J.R., *J. Am. Chem. Soc.* **2003**, *125,* 475-482.

106. Ganapathy, V., Karunagaran, B., Rhee, S., *J. Power Sources.* **2010**, *195,* 5138-5143.

107. Fabregat-Santiago, F., Garcia-Canadas, J., Palomares, E., Clifford, J.N., Haque, S.A., Durrant, J.R., Garcia-Belmonte, G., Bisquert, J., *J. Appl. Phys.* **2004**, *96,* 6903-6907.

108. O'Regan, B.C., Scully, S., Mayer, A.C., Palomares, E., Durrant, J., *J. Phys. Chem. B.* **2005**, *109,* 4616-4623.

109. Lin, C., Tsai, F., Lee, M., Lee, C., Tien, T., Wang, L., Tsai, S., *J. Mater. Chem.* **2009**, *19,* 2999-3003.

110. Zhang, X., Sutanto, I., Taguchi, T., Tokuhiro, K., Meng, Q., Rao, T.N., Fujishima, A., Watanabe, H., Nakamori, T., Uragami, M., *Sol. Energ. Mat. Sol. Cells.* **2003**, *80,* 315-326.

111. Roelofs, K.E., Brennan, T.P., Dominguez, J.C., Bailie, C.D., Margulis, G.Y., Hoke, E.T., McGehee, M.D., Bent, S.F., *J. Phys. Chem. C.* **2013**, *117,* 5584-5592.

112. Brennan, T.P., Bakke, J.R., Ding, I., Hardin, B.E., Nguyen, W.H., Mondal, R., Bailie, C.D., Margulis, G.Y., Hoke, E.T., Sellinger, A., McGehee, M.D., Bent, S.F., *Phys. Chem. Chem. Phys.* **2012**, *14,* 12130-12140.

113. Jung, H.S., Lee, J., Nastasi, M., Lee, S., Kim, J., Park, J., Hong, K.S., Shin, H., *Langmuir.* **2005**, *21,* 10332-10335.

114. Diamant, Y., Chappel, S., Chen, S.G., Melamed, O., Zaban, A., *Coord. Chem. Rev.* **2004**, *248,* 1271-1276.

115. Roh, S., Mane, R.S., Min, S., Lee, W., Lokhande, C.D., Han, S., *Appl. Phys. Lett.* **2006**, *89,* 253512/1-253512/3.

116. Diamant, Y., Chen, S.G., Melamed, O., Zaban, A., *J. Phys. Chem. B.* **2003**, *107,* 1977-1981.

117. Thavasi, V., Renugopalakrishnan, V., Jose, R., Ramakrishna, S., *Mater. Sci. Eng. , R.* **2009**, *R63,* 81-99.

118. Chen, S.G., Chappel, S., Diamant, Y., Zaban, A., *Chem. Mater.* **2001**, *13,* 4629-4634.

119. Lee, S., Kim, J.Y., Hong, K.S., Jung, H.S., Lee, J., Shin, H., *Sol. Energ. Mat. Sol. Cells.* **2006**, *90,* 2405-2412.

120. Zhang, J. and Zaban, A., *Electrochim. Acta.* **2008**, *53,* 5670-5674.

121. Zhang, L., Shi, Y., Peng, S., Liang, J., Tao, Z., Chen, J., *J. Photochem. Photobio. A.* **2008**, *197,* 260-265.

122. Prasittichai, C. and Hupp, J.T., *J. Phys. Chem. Lett.* **2010**, *1,* 1611-1615.

123. Li, T.C., Góes, M.S., Fabregat-Santiago, F., Bisquert, J., Bueno, P.R., Prasittichai, C., Hupp, J.T., Marks, T.J., *J. Phys. Chem. C.* **2009**, *113,* 18385-18390.

124. Kosmulski, M., *Langmuir.* **1997**, *13,* 6315-6320.

125. Robertson, J., *J. Vac. Sci. Technol. , B.* **2000**, *18,* 1785-1791.

126. Wilk, G.D., Wallace, R.M., Anthony, J.M., *J. Appl. Phys.* **2001**, *89,* 5243-5275.

127. Chun, W., Ishikawa, A., Fujisawa, H., Takata, T., Kondo, J.N., Hara, M., Kawai, M., Matsumoto, Y., Domen, K., *J. Phys. Chem. B.* **2003**, *107,* 1798-1803.

128. Robertson, J., *Rep. Prog. Phys.* **2006**, *69,* 327-396.

129. Liu, G., Jaegermann, W., He, J., Sundström, V., Sun, L., *J. Phys. Chem. B.* **2002**, *106,* 5814-5819.

130. Zhu, W.J., Ma, T., Tamagawa, T., Kim, J., Di, Y., *IEEE Electron Device Lett.* **2002**, *23,* 97-99.

131. Houssa, M., Tuominen, M., Naili, M., Afanas'ev, V., Stesmans, A., Haukka, S., Heyns, M.M., *J. Appl. Phys.* **2000**, *87,* 8615-8620.

132. Pinna, N., Garnweitner, G., Antonietti, M., Niederberger, M., *Adv. Mater.* **2004**, *16,* 2196-2200.

133. Bredenbeck, J. and Hamm, P., *Rev. Sci. Instrum.* **2003**, *74,* 3188-3189.

134. Bonhote, P., Dias, A., Papageorgiou, N., Kalyanasundaram, K., Grätzel, M., *Inorg. Chem.* **1996**, *35,* 1168-1178.

135. Ichinose, I., Senzu, H., Kunitake, T., *Chem. Mat.* **1997**, *9,* 1296-1298.

136. Hamann, T.W., Farha, O.K., Hupp, J.T., *J. Phys. Chem. C.* **2008**, *112,* 19756-19764.

137. Chandiran, A.K., Tetreault, N., Humphry-Baker, R., Kessler, F., Baranoff, E., Yi, C., Nazeeruddin, M.K., Gratzel, M., *Nano Lett.* **2012**, *12,* 3941-3947.

138. Puurunen, R.L., *J. Appl. Phys.* **2005**, *97,* 121301/1-121301/52.

139. Kukli, K., Ritala, M., Sajavaara, T., Keinonen, J., Leskela, M., *Chem. Vap. Deposition.* **2002**, *8,* 199-204.

140. Kukli, K., Ritala, M., Leskela, M., *J. Electrochem. Soc.* **1995**, *142,* 1670-1675.

141. Putkonen, M., Sajavaara, T., Niinistoe, L., Keinonen, J., *Anal. Bioanal. Chem.* **2005**, *382,* 1791-1799.

142. Atkins,P. and de Paula,J., *Physical Chemistry,* 7th. Edition, Oxford University Press, Oxford, New York, USA, 2002.

143. http://rsl.eng.usf.edu/Documents/Tutorials/PEScalibration.pdf, retrieved June 24th, 2013.

144. Rulliére,C., *Femtosecond laser pulses: Principles and experiments.* Springer, New York, US, 2003.

145. Ames,J. and Hoff,A.J., *Biophysical Techniques in Photosynthesis.* Springer, New York, US, 2004.

146. Rensmo, H., Lunell, S., Siegbahn, H., *J. Photochem. Photobiol. A.* **1998**, *114,* 117-124.

147. Yamakata, A., Ishibashi, T.-, Onishi, H., *Chem. Phys. Lett.* **2001**, *333,* 271-277.

148. Berger, T., Anta, J.A., Morales-Florez, V., *J. Phys. Chem. C.* **2012**, *116,* 11444-11455.

149. Moser, J.E., Noukakis, D., Bach, U., Tachibana, Y., Klug, D.R., Durrant, J.R., Humphry-Baker, R., Grätzel, M., *J. Phys. Chem. B.* **1998**, *102,* 3649-3650.

150. Skinner, D.E., Colombo, D.P., Cavaleri, J.J., Bowman, R.M., *J. Phys. Chem.* **1995**, *99,* 7853-7856.

151. Lakowicz,J.R., *Principles of Fluorescence Spectroscopy,* 3rd. Edition, Springer, New York, USA, 2006.

152. Lehtivuori,H., *Photodynamics of Energy and Electron Transfers in Solid Films of Porphyrin, Phthalocyanine, and Perylene Diimide Derivatives,* PhD Thesis, Tampere University of Technology, 2010.

153. Miettunen, K., Halme, J., Toivola, M., Lund, P., *J. Phys. Chem. C.* **2008**, *112,* 4011-4017.

154. Fabregat-Santiago, F., Bisquert, J., Palomares, E., Otero, L., Kuang, D., Zakeeruddin, S.M., Grätzel, M., *J. Phys. Chem. C.* **2007**, *111,* 6550-6560.

155. Bisquert, J., *Phys. Chem. Chem. Phys.* **2003**, *5,* 5360-5364.

156. Barsoukov,E. and Macdonald,J.R., *Impedance Spectroscopy - Theory, Experiment, and Applications,* 2nd. Edition, John Wiley & Sons, Inc., New Jersey, US, 2005.

157. Zewail, A.H., *J. Phys. Chem. A.* **2000**, *104,* 5660-5694.

158. Mäkinen, V., Honkala, K., Häkkinen, H., *J. Phys. Chem. C.* **2011**, *115,* 9250-9259.

159. Barbe, C.J., Arendse, F., Comte, P., Jirousek, M., Lenzmann, F., Shklover, V., Grätzel, M., *J. Am. Ceram. Soc.* **1997**, *80,* 3157-3171.

160. Lazzeri, M., Vittadini, A., Selloni, A., **2001**, *63,* 155409/1-155409/9.

161. Gutmann, S., Wolak, M.A., Conrad, M., Beerbom, M.M., Schlaf, R., *J. Appl. Phys.* **2010**, *107,* 103705/1-103705/8.

162. Henrich,V.E. and Cox,P.A., *The Surface Science of Metal Oxides,* Edition, Cambridge University Press, New York, US, 1994.

163. Suzer, S., Sayan, S., Banaszak Holl, M.M., Garfunkel, E., Hussain, Z., Hamdan, N.M., **2003**, *21,* 106-109.

164. Bisquert, J., Garcia-Belmonte, G., Fabregat-Santiago, F., Ferriols, N.S., Bogdanoff, P., Pereira, E.C., *J. Phys. Chem. B.* **2000**, *104,* 2287-2298.

165. Law, M., Greene, L.E., Radenovic, A., Kuykendall, T., Liphardt, J., Yang, P., *J. Phys. Chem. B.* **2006**, *110,* 22652-22663.

166. Shanmugam, M., Baroughi, M.F., Galipeau, D., *Thin Solid Films.* **2010**, *518,* 2678-2682.

ORIGINAL PAPERS

I

ELECTRON INJECTION STUDIES OF DYE-SENSITIZED TiO_2 FILMS IN SOLVENT AND IN IODIDE/TRIIODIDE ELECTROLYTE: EVIDENCE OF DYE REGENERATION IN THE PICOSECOND TIMESCALE

by

Liisa J. Antila, Pasi Myllyperkiö, Satu Mustalahti, Heli Lehtivuori and Jouko Korppi-Tommola, 2013

manuscript

https://doi.org/10.1021/jp4124277

II

SUPPRESSION OF FORWARD ELECTRON INJECTION FROM $RU(DCBPY)_2(NCS)_2$ TO NANOCRYSTALLINE TIO_2 FILM AS A RESULT OF AN INTERFACIAL AL_2O_3 BARRIER LAYER PREPARED WITH ATOMIC LAYER DEPOSITION

by

Liisa J. Antila, Mikko J. Heikkilä, Viivi Aumanen, Marianna Kemell, Pasi Myllyperkiö, Markku Leskelä, and Jouko E. I. Korppi-Tommola, 2010

Journal of Physical Chemistry Letters, vol 1, 536-539

https://doi.org/10.1021/jz9003075

III

ALD GROWN ALUMINUM OXIDE SUBMONOLAYERS IN DYE-SENSITIZED SOLAR CELLS: THE EFFECT ON INTERFACIAL ELECTRON TRANSFER AND PERFORMANCE

by

Liisa J. Antila, Mikko J. Heikkilä,Ville Mäkinen, Niko Humalamäki, Mikko Laitinen, Veikko Linko, Pasi Jalkanen, Jussi Toppari, Viivi Aumanen, Marianna Kemell, Pasi Myllyperkiö, Karoliina Honkala,Hannu Häkkinen, Markku Leskelä, and Jouko E. I. Korppi-Tommola, 2011

Journal of Physical Chemistry C, vol 115, 16720–16729

https://doi.org/10.1021/jp204886n